Characterizing Extreme Compositions on the Moon Using Thermal Infrared Spectroscopy

Nandita Kumari[1,2], Laura B. Breitenfeld[2,3], Katherine Shirley[4] and Timothy D. Glotch[5]
[1]Department of Earth, Environmental and Planetary Sciences, Brown University, [2]Planetary Science Institute, [3]Department of Astronomy, Mount Holyoke College, [4]Department of Atmospheric, Oceanic and Planetary Physics, University of Oxford, [5]Department of Geosciences, Stony Brook University

Abstract

The ultramafic and silicic rocks on the lunar surface have played an important role in expanding our knowledge regarding its thermal and magmatic evolution. The surface identification and quantification of these rocks on the global scale can significantly improve our understanding of their spatial extents, relationships and formation mechanisms. Christiansen feature positions using Diviner data have aided in global identification and mapping of relatively silica-rich and silica-poor lithologies on the lunar surface. We have used laboratory thermal infrared spectra of silicic and ultramafic rocks to analyze the variation in Christiansen feature in simulated lunar environment. We have characterized the absolute bulk silica content of the rocks and minerals and their Silica, Calcium, Ferrous iron, Magnesium index. We find that they are linearly correlated to the Christiansen feature despite particle size variations. Furthermore, we find that the Christiansen feature shifts towards longer wavelengths with increase in ilmenite content in the ilmenite-basalt mixtures. We have explored the effect of instrument's spectral band position on the accuracy of the parabolic method that is currently used for the estimation of Christiansen feature position from Diviner data. We find that this

method performs poorly for the estimation of the Christiansen feature for ultramafic and silicic rocks and minerals/mineral mixtures. We propose using a machine learning algorithm to estimate the Christiansen feature with higher accuracy for all kinds of silicate compositions on the Moon. This method will lead to increased accuracy in absolute quantification of bulk silicate composition of the lunar surface at varying spatial scales.

Plain Language Summary

Quantification of silicic and ultramafic compositions such as granites and ilmenite-rich basalts is very important to advance the understanding of temporal and thermal evolution of the Moon and for in-situ resource utilization. Silicic rocks, also known as granitic rocks, typically form on Earth near tectonic plate boundaries. However, since the Moon lacks such boundaries, their formation remains a mystery. In contrast, the presence of ilmenite-bearing rocks on the Moon is linked to the possible existence of a rare Earth element-rich layer beneath the lunar crust. The extent of this layer is still debated, yet it plays a crucial role in understanding the Moon's compositional and thermal evolution. While the returned samples and orbital datasets confirm their presence on the surface of the Moon, robust quantification techniques need to be designed to decipher their extent and formation mechanism on the lunar surface. In this paper, we have tried to bridge the gap between the laboratory measurements and orbital observations as

well as leverage artificial intelligence tools to design models to quantify these compositions on the Moon.

Key Points

- Christiansen feature shifts to longer wavelengths with increase in ilmenite in ilmenite-basalt mixtures.
- Christiansen feature cannot quantify SiO_2 wt.%. Silica, Calcium, Ferrous iron, Magnesium index is accurate for quantification of bulk silica.
- Machine learning for Christiansen feature position estimation is crucial for absolute quantification of extreme lunar compositions.

1. Introduction

The composition of the lunar surface has been extensively studied using the wealth of data collected by telescopic, crewed, orbiter and lander missions (e.g., Whitaker et al., 1972; Ryder et al., 1975; Staid et. al., 2011; Klima et al., 2011; Glotch et al.,2010). These datasets along with the returned samples and meteorites have shaped our current understanding of the thermal and magmatic evolution of the Moon after its formation (Papike et al., 1974; Papike et al., 1976; Korotev et al.,2003; Korotev,2005; Joy et al.,2013; Gross et al., 2014). The anorthositic highlands have been hypothesized to have formed as result of cooling of the lunar magma ocean (LMO) (Smith et al., 1970; Wood et al., 1970; Snyder et al., 1992; Shearer & Papike, 1999) followed by secondary basaltic volcanism driven by

mantle melting (e.g., Head & Wilson, 2017; Wilson & Head, 2017). The LMO hypothesis proposes formation of an olivine and orthopyroxene rich mantle layer and floatation of plagioclase crust leaving a residual silicate melt (Snyder et al., 1992; Shearer & Papike, 1999). This is followed by formation of KREEP(potassium, rare-Earth elements and phosphorus), enriched layer, proposed to be the source of observed ilmenite ($FeTiO_3$) in some lunar mare. There is a lack of consensus on the extent of this layer under the lunar crust and mantle overturn caused by the gravitational instability due to the high density of the layer as a result of iron and titanium (Tronche at al., 2008). Ilmenite, thus, is an extremely important mineral to understand the temporal evolution of lunar mantle and for in-situ resource utilization. It has been abundantly observed (up to ~18 wt.%) in Apollo samples with basalt (e.g., Delano and Livi, 1981; Elkins-Tanton et al., 2002; Thacker et al., 2009; Robertson et al., 2023) and several studies have been carried out to map the abundance of titanium oxide primarily present as ilmenite in the lunar mare (Blewett et al., 1997; Gillis et al., 2003; Lucey et al., 1998; Sato et al., 2017). These studies utilize the increase in reflectance of ilmenite below ~500 nm to map the spatial extent of ilmenite on the lunar surface in ultraviolet and visible-near infrared (VNIR) wavelengths (Blewett et al., 1997; Gillis et al., 2003; Sato et al., 2017). The TiO_2 wt.% estimated using these methods are affected by several factors such as albedo, space weathering and particle size (Thacker et al.,

2009; Pieters et al., 2000). Here we have acquired simulated lunar environment (SLE) spectra of Columbia River flood basalt mixed with varying ilmenite contents to understand the effects of ilmenite on the emissivity maximum position of mafic rocks in the thermal infrared (TIR).

Whitaker (1972) used ultraviolet and IR images of the full Moon by increasing color variation and decreasing albedo differences to identify anomalously red spots of substantially different composition on the lunar surface. Measurements from the Diviner Lunar Radiometer instrument (Paige et al., 2009) onboard the Lunar Reconnaissance Orbiter (LRO) ascertained the silicic (>60 wt.%) composition of the "red spots" on the lunar surface. Greenhagen et al., (2010) and Glotch et al., (2010) identified kilometer-scale volcanic complexes with lower Christiansen feature (CF) wavelength positions in the TIR on the lunar surface using Diviner data. These complexes are primarily concentrated on the nearside of the Moon within the Procellarum KREEP terrane (PKT). Glotch et al., (2010) further concluded them to be of silicic composition by confirming their spatial correlation with high-Th anomaly and low FeO content. Further studies have discerned the presence of both extrusive and intrusive silicic complexes and characterized their morphology in detail leading to the identification of felsic pyroclastic deposits and silicic batholiths (Glotch et al., 2021; Siegler et al., 2023; Qiu et al., 2023; Kumari et al., 2024b). Their presence amidst basaltic lava in the absence of plate tectonics

and lower water content and a paucity of their representative composition in the returned samples have baffled scientists for decades. The two mechanisms proposed for the formation of these rocks are: 1) silicate liquid immiscibility (SLI) (Rutherford et al., 1975; Ryder et al., 1975) and 2) basaltic underplating (Lawrence et al., 2005; Hagerty et al., 2006). SLI occurs when extreme fractionation of lunar magma results in gravity-separated layers of Fe- and Si-rich residual melts between an anorthositic roof and mafic cumulates floor. It is also believed that the separation of the residual melt from the LMO has not happened globally, and granites are present in pockets throughout the lunar crust. These can be brought to the surface by impact excavation.

The basaltic underplating hypothesis suggests that lunar silicic volcanoes result of extrusion of silicic magma with elevated thorium content formed via melting of the anorthisitic crust due to underplating by hot basaltic magma bodies. Lawrence et al., (2005) further argued that SLI is not achievable for such large volumes of magma. Silicic volcanoes, typically form on Earth in orogenic settings (Shand, 1927; Thornton and Tuttle, 1960; O'connor, 1965; Chappell and White,1974; Frost et al., 2001; Moyen et. al., 2017). However, since the Moon is a one-plate body, their existence on the lunar surface remains an enigma. In contrast, the presence of ilmenite-bearing rocks on the Moon is linked to the KREEP layer beneath the lunar crust. This layer has played a crucial role in understanding the Moon's

126 compositional and thermal evolution. Currently, we use CF as a proxy for
127 qualitative differences in SiO_2 wt.% on the Moon.

128 In addition to thermal and magmatic evolution the Moon, these two lithologies
129 (red spots and ilmenite rich basalts) may also be important for in-situ resource
130 utilization (ISRU) on the Moon. Availability of water and solar energy is of utmost
131 importance for the sustainable presence of humans on the lunar surface (e.g. NRC
132 2007; Bussey et al., 2010; Mazarico et al., 2011; Kumari et al.,2022). Water has
133 been detected to be present in higher abundance in the permanently shadowed
134 regions in the lunar poles and pyroclastic deposits on the lunar surface from
135 samples and VNIR spectra (e.g., Saal et al., 2008; Li and Milliken, 2017). Several
136 red spots host pyroclastic deposits rich in water making them important locations
137 for ISRU. However, due to the scarce presence of pyroclastic deposits (e.g., Besse
138 et al., 2014), production of water from local material has been proposed to enable a
139 long-term sustainable presence of humans on the lunar surface. Production of
140 water from reduction of ilmenite by hydrogen (H_2) has been extensively proposed
141 for this purpose (e.g., Sargent et al., 2020).

142 In this study, we have used TIR laboratory spectra, acquired in simulated lunar
143 environment (SLE) to analyze rhyolite, basalt, pumice and obsidian, i.e., rock
144 analogues to the likely compositions of red spots on the lunar surface. In addition,
145 we have prepared basalt-ilmenite mixtures to understand the variation in CF of

146 basalt with increasing ilmenite content from TIR spectra acquired in SLE. We have
147 also analyzed the accuracy of current methods used to estimate CF and relationship
148 between CF and SiO_2 wt.% as well as silica-calcium-iron-magnesium(SCFM)
149 index. We propose a supervised machine learning algorithm for CF estimation and
150 find that SCFM index performs better for bulk silica using the TIR spectra.

151 **2. Background**

152 Thermal infrared spectroscopy has been an indispensable tool for studying the
153 surfaces of rocky planets. The spectra at TIR wavelengths are a combination of
154 real index of refraction (n) and imaginary index of refraction (k) and vary with
155 individual material resulting in unique fingerprints that can be used to identify,
156 analyze and quantify them. A number of laboratory studies (e.g. Conel, 1969;
157 Logan et al., 1973; Hunt, 1977; Glotch et al., 2007; Shirley and Glotch, 2019) have
158 further expanded our understanding of the behavior of minerals and their mixtures
159 under varying physical and environmental conditions through the acquisition of
160 spectra of silicates under these conditions. These spectral libraries have also
161 enabled the identification and quantification of several minerals from orbital
162 datasets. At TIR wavelengths, coarse particle mineral mixtures tend to mix linearly
163 which enables linear unmixing of different minerals for quantification purposes
164 (Christensen and Harrison, 1993; Ramsey and Christensen, 1998; Rogers and
165 Aharonson, 2008). However, spectra of fine particles (defined as smaller than the

166 wavelength of light) mix non-linearly and radiative transfer models are used to
167 accommodate nonlinear spectral mixture analysis (e.g., Isaacson et al., 2011;
168 Robertson et al., 2022). In addition, the diagnostic features of the TIR spectral
169 datasets such as CF, Reststrahlen bands (RB) and transparency features (TF) have
170 also been used to understand the bulk composition and other physical
171 characteristics of the planetary surface (Greenhagen et al., 2010; Glotch et al.,
172 2010; Shirley et al., 2023; Kumari et al., 2024a;2024b).

173 The CF occurs where the real part of the complex refractive index passes unity
174 and serves as an indicator of silica polymerization. Its wavelength position is
175 inversely correlated to the bulk silica content of the mineral, occurring at shorter
176 wavelengths for silicic minerals and at longer wavelengths for mafic
177 minerals(Conel,1969; Logan et al., 1973; Salisbury et al., 1991; Christensen et al.,
178 2000). Due to this relationship, the CF has been used to map the bulk silicate
179 composition of the lunar surface (e.g., Greenhagen et al., 2010). However, detailed
180 laboratory studies established that in addition to bulk silicate composition, the
181 variation in CF wavelength position is also caused by particle size, albedo,
182 porosity, temperature and environmental conditions (Logan et al., 1973; Shirley
183 and Glotch, 2019; Thompson et al., 2021; Shirley et al.,2023; Kumari et al.,
184 2024a). The CF wavelength position for different mafic and felsic minerals shifts
185 to shorter wavelength in SLE compared to ambient environment; shifts to longer

186 wavelength upon decrease in particle size within SLE (e.g., Shirley and Glotch,
187 2019; Kumari et al., 2024a) and shifts to longer wavelengths with decrease in
188 albedo caused by space weathering (e.g., Shirley et al., 2023; Kumari et al., 2024).
189 Other factors that affect CF wavelength position include the porosity of the
190 material wherein CF moves to longer wavelengths with increase in porosity in
191 ambient environment (e.g., Logan et al., 1973), photometry and surface
192 temperatures (Greenhagen et al., 2011). Since CF is used to characterize
193 compositions of the surface, these factors can complicate interpretations and need
194 to be accounted for.

195 Diviner channels 3, 4 and 5, corresponding to 7.55 - 8.05 μm, 8.1 - 8.4 μm,
196 and 8.38 - 8.68 μm (Paige et al., 2009) are used to estimate CF. Diviner channels 1
197 and 2 are narrow- and broadband solar channels, respectively and channels 6-9 are
198 broadband thermal channels used for temperature measurements and
199 thermophysical studies. A parabolic fit on channels 3 to 5 is carried out and the
200 maximum of the fit is assumed to be the CF of the spectrum. Since most of the
201 lunar near side surface is covered with mare basalts with CF values around ~8.2
202 μm and the farside is primarily anorthositic with CF values around ~7.8 μm
203 (Greenhagen et al., 2010) the estimated CF values are a good representative of the
204 composition. However, as the true CF of materials moves away from 8 μm in
205 either direction, the accuracy of the parabolic fit method is reduced, and ad hoc cut

offs have been placed at ~6.9 μm and ~9.6 μm by Greenhagen et al., (2010). Silicic and ultramafic compositions have CFs lying below ~7.4 μm and above ~8.4 μm respectively. Thus, in order to study these "extreme" compositions/rock types we need a more accurate method to estimate the CF wavelength position. Other three-band instruments such as Lunar Compact Infrared Imaging System (L- CIRiS) (Hayne et al., 2019) and Lunar Vulkan Imaging and Spectroscopy Explorer(L-VISE) (Donaldson Hanna et al., 2023) will encounter the same issues due to similar number and location of bands. Since CF will also be used to estimate bulk silicate compositions using these instruments, we are proposing a more robust method for CF estimation.

3. Datasets and Methods

We have used the laboratory spectra and oxide data of monomineralic samples acquired by Shirley and Glotch (2019) and Shirley et al., (2023) acquired in SLE. TIR spectra of rhyolite, obsidian, trachybasalt, pumice at seven different particle sizes (both fine to coarse grained) and fourteen basalt-ilmenite mixtures with varying ilmenite composition were acquired in SLE. The basalt-ilmenite mixture with the ilmenite content of 12 vol.% and higher displayed a carbon feature near 8.1 μm that has been removed by removing that part of the spectrum. The basalt used in this study is Columbia River basalt with particle size <63 μm (Thorpe & Hurowitz, 2020). We then mixed ilmenite (<63 μm) to the basalt in

226 increasing volume percent. The oxide content of these four felsic rocks was
227 obtained using XRF analysis and is given in supplementary information. A Nicolet
228 6700 FTIR spectrometer attached to the Planetary and Asteroid Regolith
229 Spectroscopy Environmental Chamber (PARSEC) was used to acquire the data.
230 PARSEC is an environmental simulation chamber capable of achieving
231 temperatures below 150 K through cooling via liquid nitrogen. It can achieve
232 vacuum at pressures below 10^{-4} mbar and includes a rotating wheel with six sample
233 cups, an external black body target and an internal calibration target illuminated at
234 an incidence angle of 55^{o} (Shirley and Glotch, 2019). Samples are heated from
235 above by a quartz halogen lamp and from below by individual sample cup heaters
236 to achieve the desired sample brightness temperatures and lunar-like thermal
237 gradients in the samples. The brightness temperature was estimated from the
238 radiance using the two-temperature method outlined in Ruff et al., (1997) and the
239 emissivity was estimated by ratioing the brightness temperature of the entire
240 spectrum with the values of brightness temperature near the CF (assuming
241 emissivity to be unity at CF) of each spectrum.

242 The hyperspectral data were then convolved to 3-band and 11-band spectra
243 using the instrument filter functions. We have used the in-flight filter function for
244 the Diviner channels 3, 4 and 5 (Paige et al, 2009) (Fig.1a). For the other relevant
245 upcoming missions with three bands such as L-CIRiS, L-VISE we have assumed a

boxcar response over the spectral bandwidths of each of their channels due to the current absence of their in-flight response function (Fig 1b, c). We have assumed the response described by Ehlmann et al., (2022) for 11-band Lunar Trailblazer Lunar Thermal Mapper (LTM) spectra (Fig 1d). It should be noted that the resultant convolved spectra will vary when the upcoming missions make their actual filter functions available and that will slightly affect the model parameters and resultant metrics.

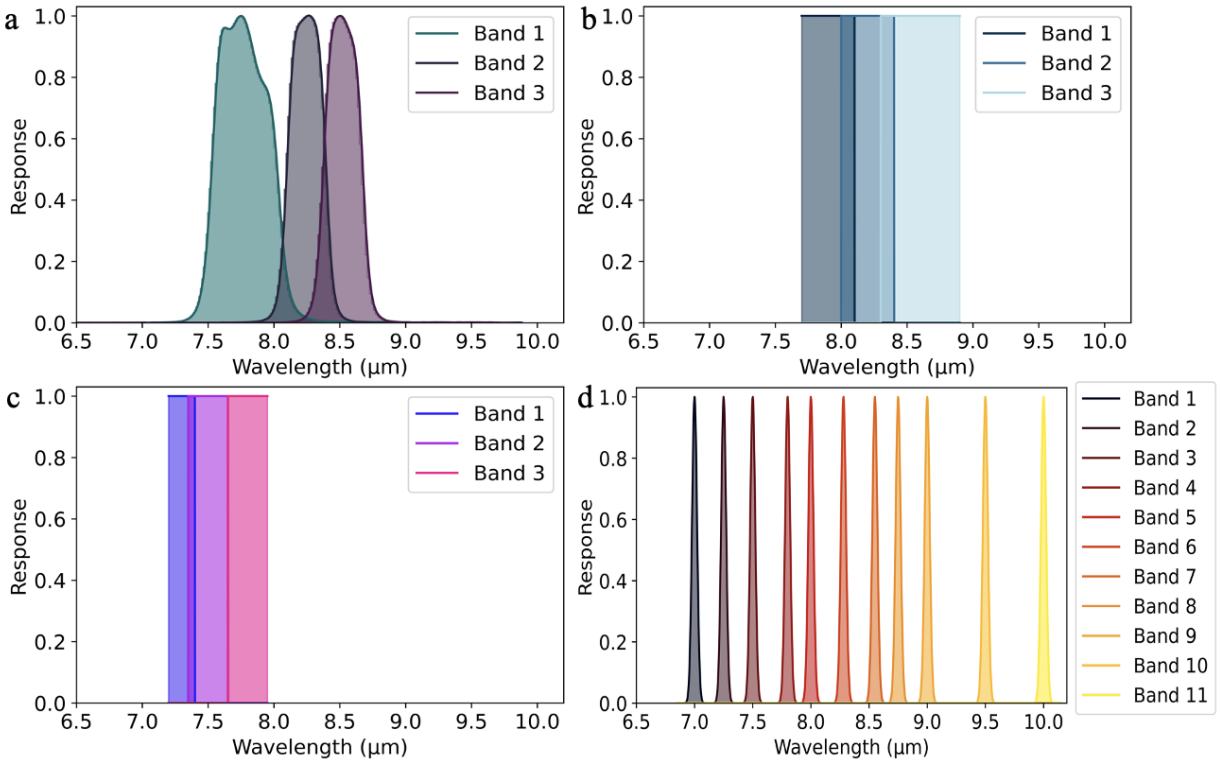

Fig. 1*a) Filter functions of three Diviner bands b) Model filter functions of three LCIRiS bands c) Model filter functions of three LVISE bands d) Model filter functions for LTM onboard Lunar Trailblazer.*

The true CF of each laboratory spectrum was estimated using a polynomial fit between 6.6 μm and 14 μm (depending on the mineral or rock composition),

similar to Shirley and Glotch (2019), near the shoulder of hyperspectral data (Fig. 2). The CFs from the convolved multispectral data were estimated using a parabolic fit similar to Greenhagen et al., (2010). In addition, we have also used a support vector regression (SVR) model to estimate CFs from the multispectral datasets.

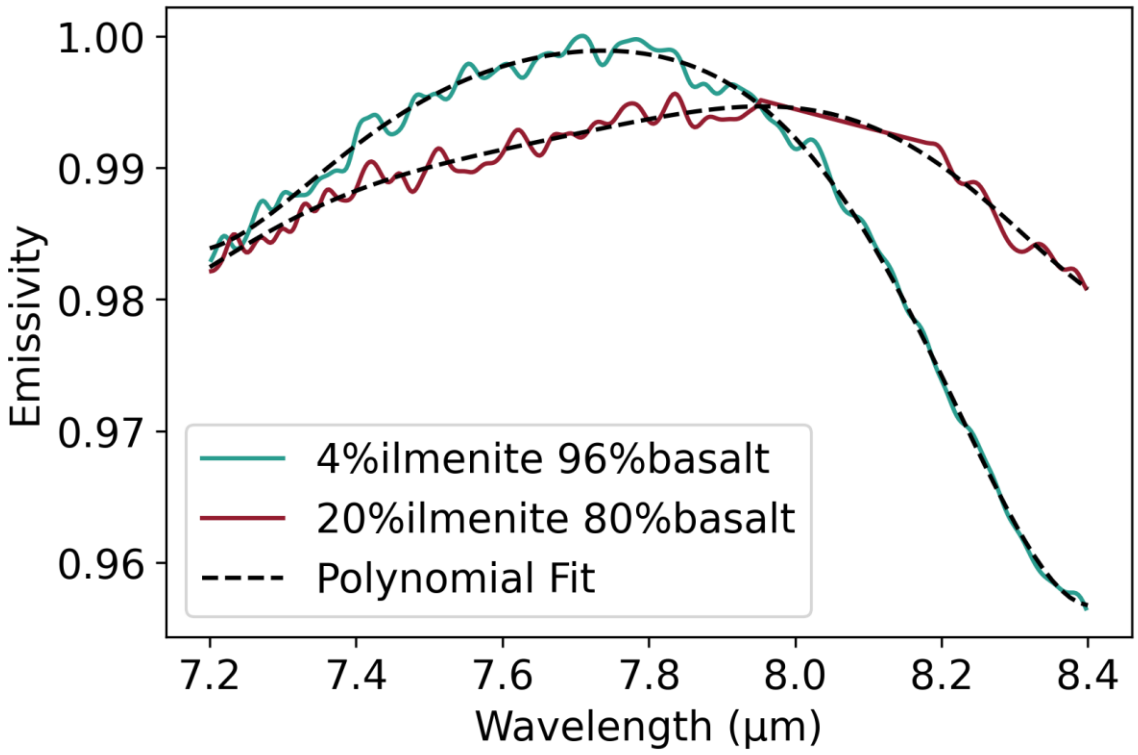

Fig 2. *Polynomial fit for the CF estimation using the method outlined in Shirley and Glotch (2019).*

SVR is a supervised machine learning algorithm based on support vector machines to be used for regression tasks(Vapnik et al.,1996). This technique uses kernels to project the data to a higher dimension to simplify (sometimes also linearize) a non-linear relationship amongst the input features (here it is the

emissivity at each band). Following that the algorithm defines a hyperplane that also defines a relationship between the spectrum and CF. It only penalizes the errors that exceed a specified threshold (margin) in terms of their distance from that plane, thus allowing for some tolerance within the prediction. The data points that lie on or within the margin are called support vectors and define the boundary (C) and other parameters, making them crucial for the determination of the optimized hyperplane. Larger C could lead to low variance and high bias (underfitting) and lower C could lead to overfitting. The predictions from unknown data (test set) are based on the distance of the input features from the hyperplane. The hyperparameters in this algorithm for polynomial kernels is C and we have decided to go with the default epsilon of 0.1. Mathematically, this hyperplane is defined by the equation:

$$w^T \mathrm{x} + \mathrm{b} = 0$$

The distance from a data point (x_i) to the plane is defined by

$$\frac{|w^T x_i + \mathrm{b}|}{||\mathrm{w}||}$$

Since, the optimized margin is the smallest distance between the data points and the hyperplane, this algorithm aims to minimize the following function

$$min \frac{1}{2} ||w||^2 + C \sum_i e_i$$

$$\text{subject to } y_i(w^T x_i + \mathrm{b}) \geq 1 - e_i \text{ where i} = 1, \ldots .n$$

where **w** is weighted vector normal to the plane, **x** is the input parameter (here spectrum), **b** is a bias term, **y** is the output parameter (here CF), **C** is regularization parameter, **e** is the threshold and **n** is the number of samples.

We have used 80% of the spectral data for training and 20% for validating the model from our spectral library of 98 spectra. The training set was then further divided into a number of subsets and a subset was held out for testing the model. This was repeated *n* times where *n* is the number of subsets and computed via the square root of the total number of samples in the training set. For our model, we used nine folds. This process is known as cross-validation (CV). For the cross-validation to work, another important factor is representation of different variations of spectral composition in each fold. While stratifying categorical data is relatively straightforward, stratifying continuous variables such as CF required innovative approaches. From trial and error, we find that sorting the values of targeted variable (CF) and then assigning folds in recurring format works the best, thus we will be using that for our folds. The model was then tested on the validation set. We have used the r-squared value and root mean squared error (RMSE) to quantify model errors. The error quantified from the predictions of training set and test set are known as RMSE_CV and RMSE_P respectively. We have trained the SVR model for each multispectral dataset separately to predict true CF values (estimated from the lab spectra) from different multispectral datasets. Following this a

relative difference in the RMSE computed using parabolic and ML method was estimated using the following formula:

$$\text{Relative difference} = \frac{abs(RMSE\_P - RMSE\_parabolic\_fit)}{RMSEP}$$

We have used linear regression to understand the correlation between 1) CF versus SCFM and 2) CF versus SiO_2 wt.%.

4. Results

4.1 CF of Silicic Rocks and Basalt-Ilmenite Mixtures

The spectra of felsic rocks in SLE display CF at short wavelengths.

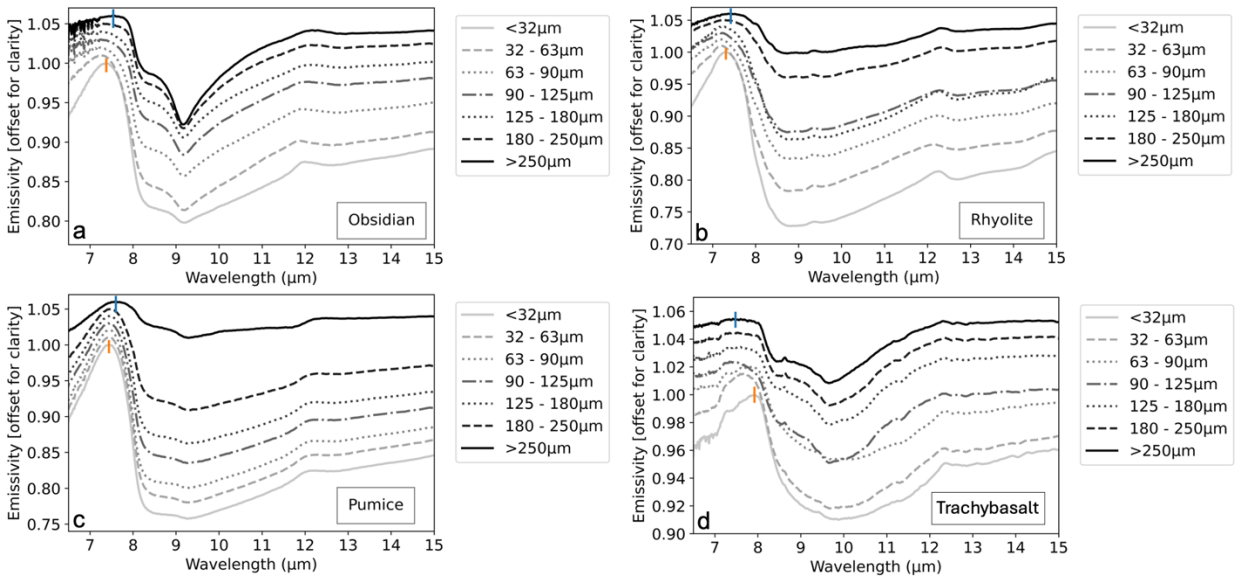

Fig. 3 *TIR spectra of (a) obsidian, (b) rhyolite, (c) pumice, and (d) trachybasalt at seven different particle sizes. The orange and blue markers in each image displays the CF position of the finest and coarsest fraction of each rock type.*

The obsidian, rhyolite and pumice have 74.76 wt.%, 71.69 wt.% and 68.35 wt.% SiO_2 content respectively. The CF of obsidian lies at ~7.38 μm for particles below 32 μm and at ~7.54 μm for particles above 250 μm. We observe a narrow

RB around ~9.17 μm with increasing width and decreasing contrast as the particle size increases (Fig. 3a). The CF of rhyolite lies at longer wavelength for larger particle sizes (~7.42 μm for >250 μm) than for smallest particle size fraction (~7.31 μm for <32 μm). However, this increase in CF with particle size is not linear and we observe a decrease in CF for particle sizes below 250 μm and above 32 μm. The RB for rhyolite lies near ~8.7 μm and we observe an increase in contrast with decrease in particle size (Fig. 3b). The pumice displays CF wavelength position at ~7.44 μm at finer particle size (<32 μm) and that shifts to longer wavelength at ~7.6 μm for coarser particles (>250 μm). The RB wavelength position lies near ~9.3 μm and we observe an increase in contrast with decrease in particle size consistent with other felsic rocks (Fig. 3c). We do not observe a linear increase or decrease in the CF or RB values at smaller or larger particles with increasing SiO_2 wt.% amongst the three rocks. The CF position of trachybasalt with SiO_2 content of 45.45 wt.% lies at the longest wavelengths amongst all of the above rocks and moves to shorter wavelengths with increase in particle size. The smallest particle size (<32 μm) has CF wavelength position at ~7.92 μm while CF lies at ~7.48 μm for particles greater than 250 μm. The RB for trachybasalt lies near ~9.7 μm with a consistent decrease in emissivity as the particle size deceases (Fig. 3d).

We have used ilmenite-basalt mixtures to understand the effect of increasing ilmenite content on the CF and RB wavelength positions of basalt. The basalt (LC001) used in this study was collected from Grande Ronde in the Columbia River Basalt region and contains 63.6 wt.% Plagioclase, 26.0 wt.% Pyroxene, 1.7 wt.% Olivine, 1.4 wt.% Fe/Ti Oxides, and 7.3 wt.% amorphous material(Thorpe and Hurowitz, 2020). The CF wavelength position of the basalt lies at ~7.66 μm and RB wavelength near ~9.09 μm. The CF wavelength positions of the basalt-ilmenite mixtures are at ~7.73 μm (4 vol.% ilmenite and 96 vol.% basalt), ~7.82 μm (8 vol.% ilmenite and 92 vol.% basalt), ~8.01 μm (12 vol.% ilmenite and 88 vol.% basalt), ~8.03 μm (14 vol.% ilmenite and 86 vol.% basalt), and ~8.05 μm (20 vol.% ilmenite versus 80 vol.% basalt) (Fig. 4). The RB wavelength position varies between the ~9.09 μm and ~9.14 μm for these mixtures and we observe a consistent increase in emissivity and decrease in contrast of the RB wavelength with increase in ilmenite content (Fig. 4). The mixtures were created to represent the quantity of ilmenite observed on the lunar surface through Apollo samples and remote sensing. We observe a consistent increase in CF wavelength position with an increase in the ilmenite content in the mixtures (Fig. 4).

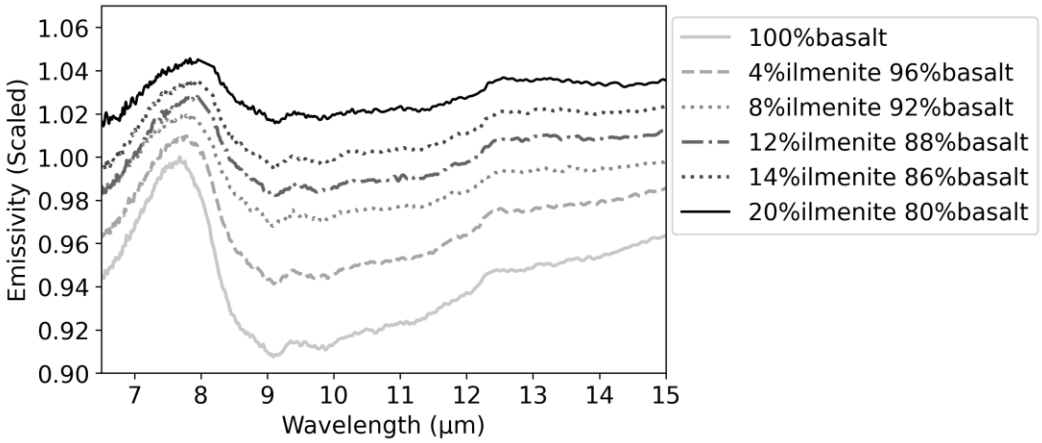

Fig. 4 *TIR spectra of ilmenite-basalt mixtures with increasing ilmenite content.*

4.2 Ongoing and Upcoming Missions

We convolved the laboratory spectral data from Shirley and Glotch (2019) and our work to the spectral sampling of the Diviner, LCIRiS, LVISE and LTM observations using the Diviner filter functions and model filter functions for the other instruments.

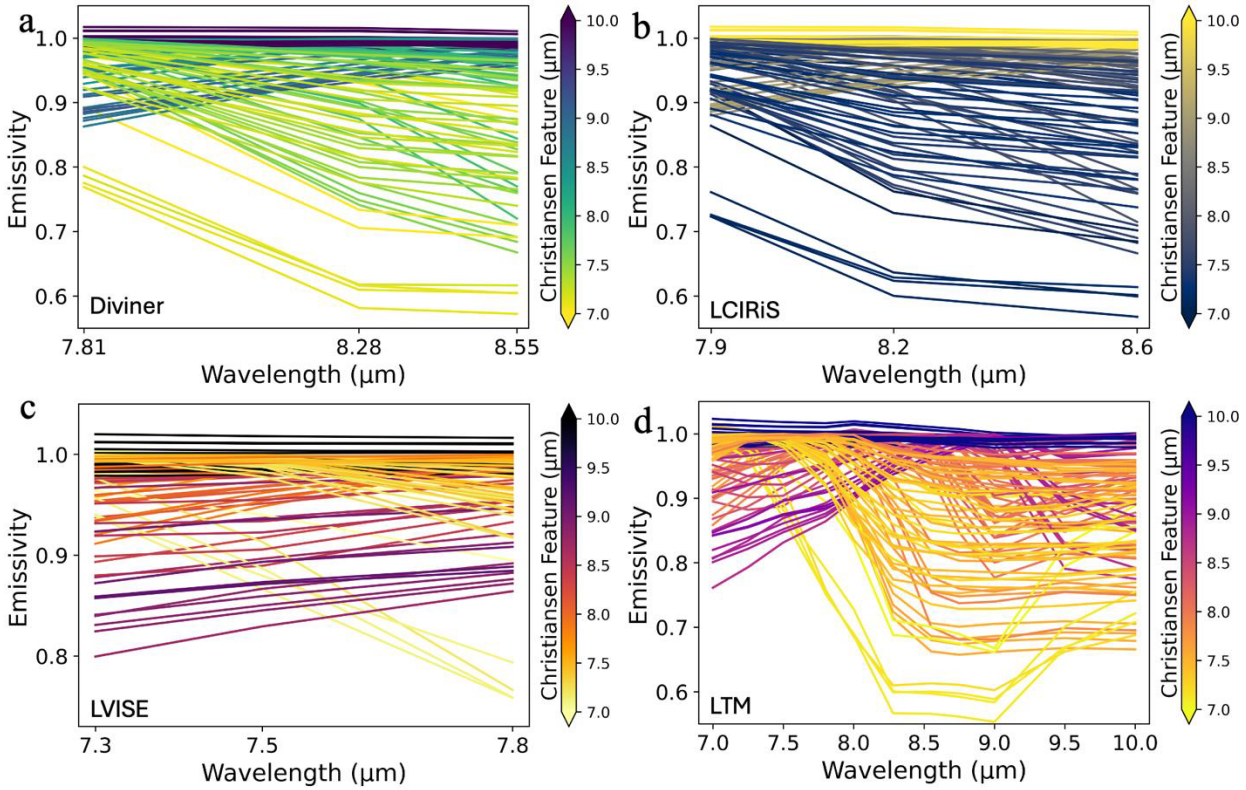

Fig. 5 *Convolved mineral spectra from Shirley and Glotch (2019) and this study for a) Diviner bands b) LCIRiS bands c) LVISE bands d) LTM bands*

Our observations indicate that with Diviner convolution, the spectra with CF positions at longer wavelengths (>8.5 μm) display positive slope or appear flat (as a straight line) while other minerals with CF at shorter wavelengths display negative slopes (Fig. 5a). A similar trend was observed in the three-point convolved spectra for L-CIRiS (Fig. 5b). The convolved spectra for LVISE display a negative slope for spectra with CF position at shorter wavelengths and a positive slope followed by flattening with increase in CF position towards longer wavelengths (Fig. 5c). The convolved spectra for LTM have eleven bands and can capture the variation in CF and RB wavelength positions with variation in silica

content of different minerals with more clarity than the three-point datasets (Fig. 5d). However, we observe that the spectra do not capture the RB wavelength positions of ultramafic minerals such as forsterite or fayalite (with CF values near ~9 μm).

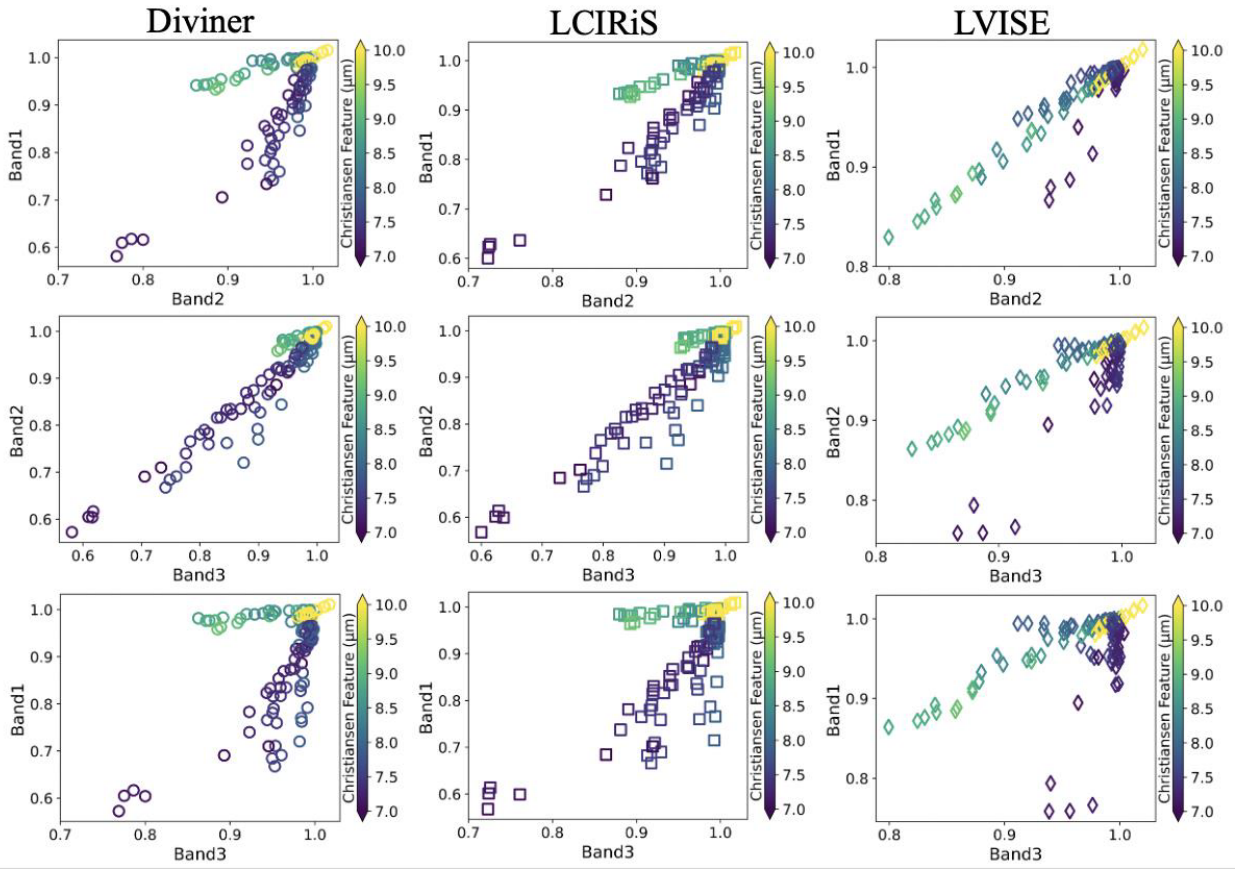

Fig. 6 *Band 1 versus Band 2 emissivity values for a) Diviner convolved spectra b) LCIRiS convolved spectra c) LVISE convolved spectra. Band 2 versus Band 3 emissivity values for a) Diviner convolved spectra b) LCIRiS convolved spectra c) LVISE convolved spectra. Band 1 versus Band 3 emissivity values for a) Diviner convolved spectra b) LCIRiS convolved spectra c) LVISE convolved spectra.*

To further our understanding, we conducted a comprehensive analysis of the emissivity values across the bands of the three instruments. This enabled us to qualitatively identify and compare any potential connections between emissivity

patterns and the CF wavelength position. For Diviner-convolved spectra, we observe that channel 3(band 1) displays higher emissivity for minerals with CFs at longer wavelengths for varying values of channels 4 (band 2) and 5 (band 3), and lower emissivity for minerals with CFs at shorter wavelengths (Fig. 6a, g). We observe a similar relationship between emissivities of band 1 versus bands 2 and 3 and CF wavelength position for LCIRiS (Fig. 6b, h, i). We do not observe this in band 1 versus band 2 or band 1 versus band 3 for LVISE (Fig. 6c). No distinct pattern emerges for channel 4 (band 2) vs channel 5 (band 3) for Diviner data (Fig. 6d). For LCIRiS, the band 2 versus band 3 emissivity values also plot distinctly for minerals with CF at longer and shorter wavelengths with band 2 emissivity being higher for ultramafic minerals compared to felsic minerals (Fig. 6e). This trend is also observed in band 2 versus band 3 emissivity of LVISE (Fig. 6f).

4.3 CF Estimation - Parabolic Estimation and Machine Learning

The convolved spectra for the three band instruments were used to estimate CF using the parabolic fit method (Greenhagen et al., 2010). The method uses a parabolic fit over the three points of the spectrum and assumes the maximum of the parabola to be the CF and its corresponding wavelength position to be the CF wavelength position.

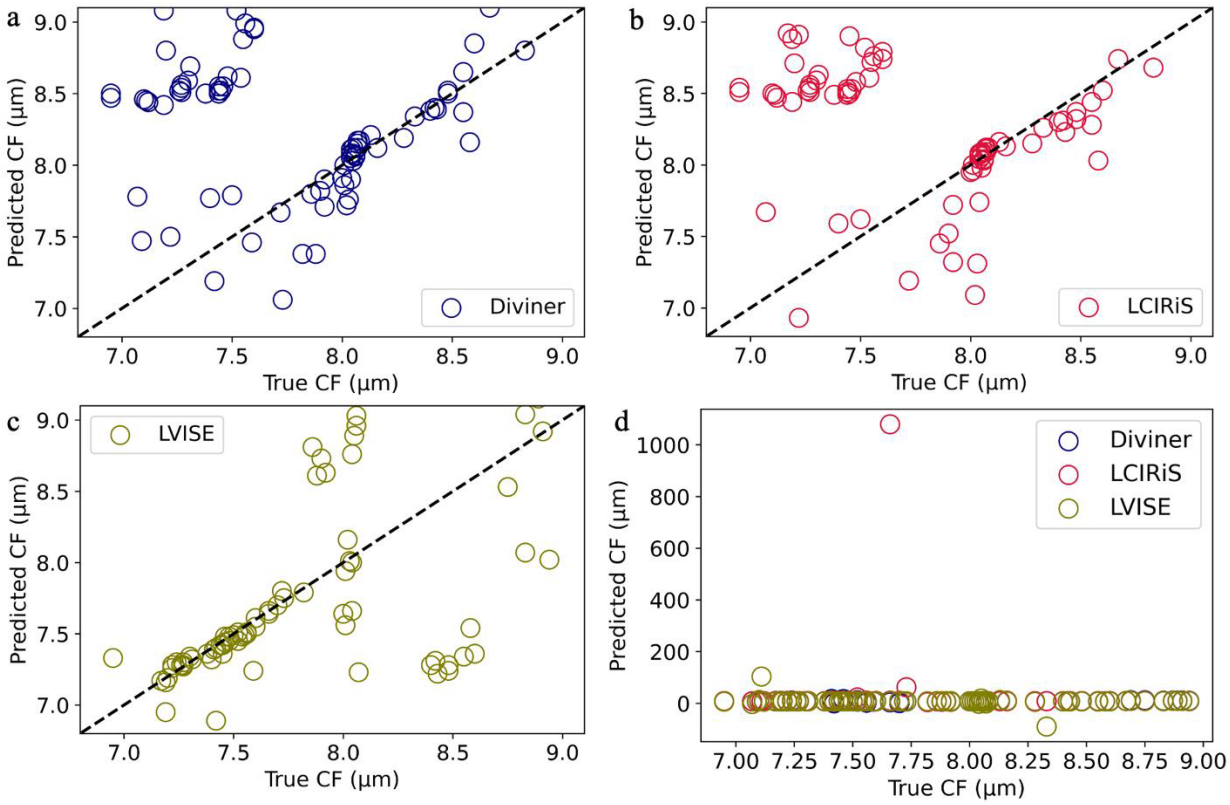

Fig. 7 *CF estimated using parabolic fit up to a value of 9 μm for (a) Diviner convolved spectra (b) LCIRiS convolved spectra (c) LVISE convolved spectra and (d) all the instrument data over the full value range. The extreme outliers here are not showed in other panels.*

CF estimated via parabolic fit for the Diviner dataset displays a linear correlation between the true and estimated value between 8.0 μm to 8.4 μm (Fig. 7a). The values beyond this range do not display any linear correlation with the true CF and currently an ad-hoc cutoff has been placed at 6.9 μm and 9.6 μm to prevent larger errors (Greenhagen et al., 2010). The total root mean square error (RMSE) of estimated and true CF for this instrument is 2.1 μm without removing any outliers, if we remote outliers beyond three standard deviations of the dataset, the RMSE turns out to be 1.2 μm. For L-CIRiS, this linear relationship can be seen

around ~8 μm (Fig. 7b). In a manner similar to Diviner, there is no correlation beyond this range. This is because the bands used to convolve these datasets are centered around 8 μm making the prediction accuracy higher around 8 μm. The CF estimation carried out on LVISE convolved spectra displays a linear correlation between 7.2 μm to 7.8 μm since the bands are located around 7.5 μm (Fig. 7c). The RMSE for parabolic prediction using LCIRiS data is 108.38 μm and LVISE data is 14.08 μm without removing outliers. When we remove the outliers beyond three standard deviations, the RMSE of LCIRiS reduces to 5.8 μm and LVISE reduces to 2.25 μm. Fig. 7d displays the parabolic fit predictions over the three datasets without a reduced range up to 9 μm.

In addition to the parabolic fit, we also used support vector regression model to predict CF from three band and eleven band datasets. There is a linear correlation between predicted and true CF values for Diviner with the r-squared of the training set being 0.94 and the test set being 0.91 (Fig. 8a). The RMSE of the training set is 0.14 and test set is 0.14 μm (Fig. 8a). For L-CIRiS, the r-squared value for training set is 0.95 and the test set is 0.91 while the RMSE of the training set is 0.12 μm and the test set is 0.14 μm (Fig. 8b). This plot displays a linear correlation with some scatter for lower CF values. The r-squared value for the training set of L-VISE is 0.86 and test set is 0.88 while the RMSE is 0.2 μm and 0.17 μm respectively (Fig. 8c). Among the three-band instruments, the true versus

estimated CF plot of L-VISE displays the most scatter and least accuracy. The highest accuracy is displayed by LTM with least scatter and RMSE of 0.1 μm for training set and 0.09 μm for test set. The r-squared for both the sets are 0.97 and 0.96 respectively (Fig. 8d). The reason for the association between LTM and the highest accuracy is likely the result of an increase in the number of bands and thus more information for the model to generalize upon and capture the relationship between the bands and the CF position.

Mission	Relative Difference computed without outliers	Relative Difference computed with outliers
Diviner	6.4375	12.125
LCIRiS	7.85	26.35
LVISE	8.38	70.67

Table 1: Relative difference between the RMSE of CF position estimated by ML and parabolic fit on test set.

For all the datasets, we observe a linear correlation between the true and predicted CF values across different compositions. Upon comparing the errors in CF estimation by the parabolic and CF method (Table 1) , we found that the ML method was up to 6 to 70 times more accurate than the parabolic method for estimating CF values from three band instruments.

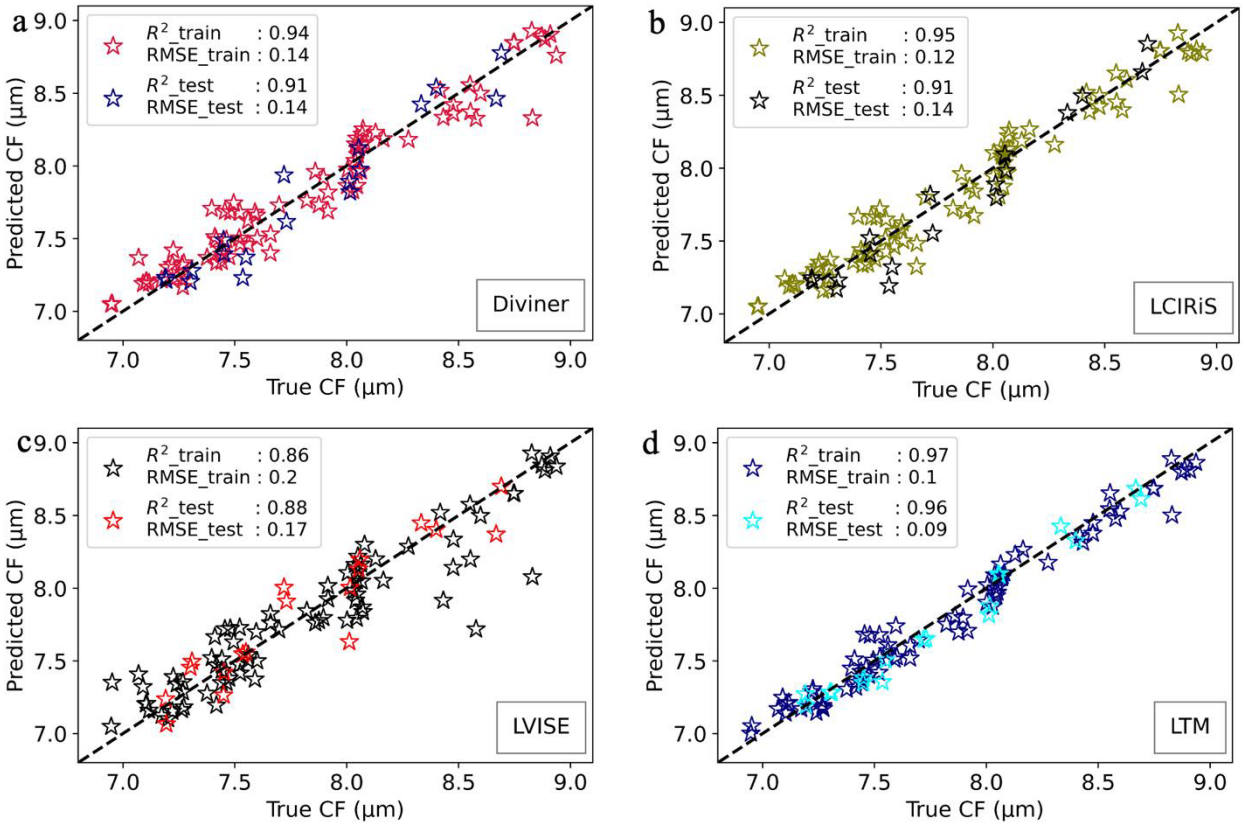

Fig. 8 *CF estimated using SVR for a) Diviner* convolved spectra *b) LCIRiS convolved spectra c) LVISE convolved spectra d) LTM convolved spectra. e) r-squared of all the ML models and f) RMSE of all the ML models.*

4.4 Estimating Bulk Silica Content using CF

While CF wavelength position serves as a good indicator of bulk silica composition, it is affected by a lot of factors such as particle size, porosity, space weathering, environment, and viewing geometry. Thus, absolute quantification of bulk silica content is of utmost importance to understand the composition of silicic volcanoes on the lunar surface. We have used SCFM index, SiO_2 wt.% and CF of various minerals at different particle sizes to quantify the bulk silica content. The

SCFM index is a ratio of silica abundance to sum of Si, Ca, Fe, Mg oxide abundance.

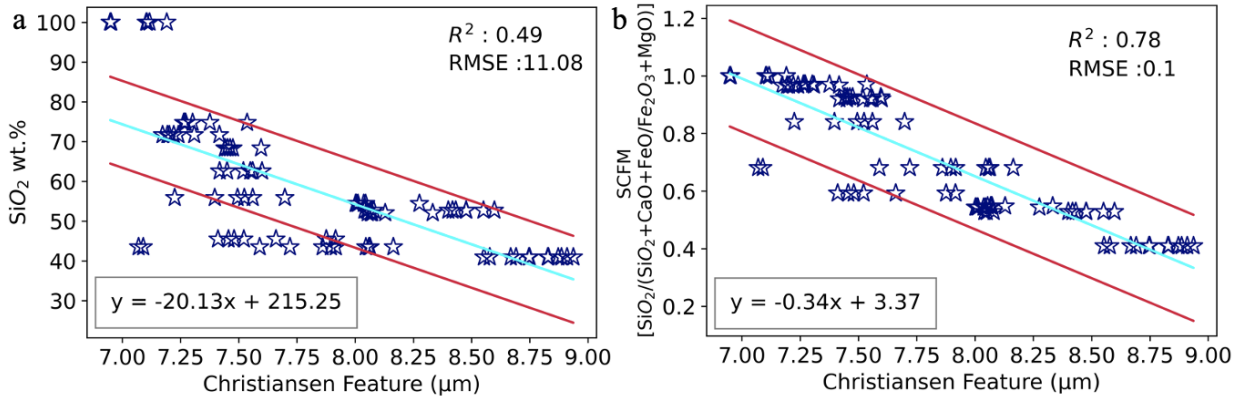

Fig. 9 *a) SiO_2 wt.% versus true CF position estimated using polynomial fit and b) SCFM index versus true CF position estimated using polynomial fit.*

We plot the CF values at different particle sizes of the different minerals in Shirley and Glotch (2019) and this study against SiO_2 wt.% and SCFM index. We observe that the CF wavelength position displays a poor linear correlation with SiO_2 wt.% when CF variation due to different particle size is included in the model (Fig. 9a). The CF Vs SiO_2 wt.% plot has a correlation coefficient of 0.48 and RMSE of 11.17 wt.% (Fig. 9a). The CF wavelength position displays a stronger correlation with SCFM index. We observe a correlation coefficient of 0.78 and RMSE of 0.1 (Fig. 9b). Most of the SCFM values fall within one standard deviation of the prediction line (Fig. 9b). The equation for estimating SCFM from CF values is

$$SCFM = -0.34CF + 3.337$$

5 Discussion

Our measurements of different silicic rock types and ilmenite-basalt mixtures indicate that CF position moves to longer wavelengths with increase in particle size from fine (<32 μm) to coarse (>250 μm), however, this is not linear. The CF and RB value of rhyolite stands out and does not follow the trend of increase in CF with decrease in SiO_2 wt.% and displays CF at smaller wavelength than obsidian despite lower SiO_2 wt.%. Amorphous materials like obsidian can be treated like "frozen silicate liquid" because they donot have time to reach a thermally equilibrated distribution through particle rearrangement due to rapid quenching (Richet and Neuville, 1992; McMillan et al., 1992). The CF position optically, is the wavelength where the real index of refraction passes unity and structurally is an indicator of Si-O-Si bond angle which decreases with decrease in silica polymerization (King et al., 2004). Increasing Al_2O_3 in the melts can also decrease polymerization in glasses with same SiO_2 content (Lee and Stebbins, 2009). However, here we observe that the Obsidian has comparable Al_2O_3 (13 wt.%) to rhyolite (14.1 wt.% Al_2O_3). It is, thus, possible that the trend we see here due to the disarrayed structure of obsidian has lower Si-O-Si bond angle causing CF at lower wavelengths despite higher SiO_2 wt.%. In addition to that, unlike Shirley and Glotch (2019), we do observe small variations in position of RB position with particle size.

503 For the basalt-ilmenite mixtures, the CF shifts to longer wavelengths with
504 increasing ilmenite content and there is a linear correlation between them. This is
505 because the bulk silica content of the mixture decreases with the increase in
506 ilmenite. Since the acquired spectra of the mixture is a non-linear combination of
507 basalt and ilmenite spectra, an increase in ilmenite content also increases the
508 contribution of ilmenite to overall spectrum shifting the CF towards longer
509 wavelengths. It should be noted, however, that this shift could be due to any
510 ultramafic mineral and thus though there is a correlation between CF shift to longer
511 wavelengths and ilmenite content, the reverse might not always be true
512 (Greenhagen et al., 2020). A shift in CF towards longer wavelength might not be
513 an indicator ilmenite presence and thus CF itself cannot be used to confirm
514 ilmenite on the lunar surface and additional visible near infrared (VNIR)
515 measurements would be required to aid in its quantification.

516 The response functions used for the upcoming 3-band missions have been
517 assumed to be similar to Diviner with varying bandwidths, so the actual accuracy
518 of parabolic and ML method of CF estimation may be slightly different than
519 presented here. The existing parabolic fit method for CF estimation using three
520 band data from Diviner, LCIRiS and LVISE works excellently for the CF values
521 located near the measurement bands. These bands for upcoming missions (LCIRiS,
522 LVISE) have mostly been chosen based on the information from remote sensing

523 analysis of the landing sites. However, the local scales at which these instruments
524 will carry out the measurements are orders of magnitude smaller than the remote
525 sensing scales (~250 m spot size of Diviner). Due to a variation in the spatial scales
526 of observations, there is always a chance of encountering unexpectedly silicic or
527 mafic materials with CF wavelength position far away from the designed bands,
528 thus, the ML-based methods are likely to provide the most accurate CF estimation
529 for these missions. However, CF is a non-unique solution when trying to identify
530 the intermediate compositions and thus direct estimation of SiO_2 wt.% using the
531 CF position should not be carried out when defining the lithologies. Though three
532 bands are not sufficient for this kind of model, 1) SCFM index value from CF
533 and/or 2) ML based estimation of SiO_2 wt.% using a combination of boresighted
534 measurements from VNIR and TIR bands could be used for bulk silica
535 quantification. For the instruments with more bands such as LTM onboard Lunar
536 Trailblazer, a direct estimate of SiO_2 wt.% from the spectra is possible but requires
537 a spectral library customized to lunar materials and environment. That is, space
538 weathered fine grained mineral mixtures or lunar regolith samples with variable
539 compositions and maturities should be added to existing SLE spectral libraries.

540 **6 Summary**

541 In this work, we have determined the CF wavelength positions of silicic
542 rocks and ilmenite-basalt mixtures. Our observations indicate that the CF for such

extreme compositions lie far away from the measurement bands of Diviner and the current parabolic fit method performs poorly in such cases. To account for this, we have used support vector regression, a supervised machine learning model, to estimate CF position from multispectral instruments. Our model predictions display a positive linear correlation with the true CF values at locations away from where the bands are centered, and they have significantly improved accuracies. This methodology, when combined with SCFM index values, will serve to be useful for deriving bulk silica content from upcoming missions by easily identifying and quantifying unusual materials on the surface of the Moon.

Data Availability Statement

The data used in this study can be accessed at Kumari et al., (2025).

References

Besse, S., Sunshine, J.M. and Gaddis, L.R., (2014). Volcanic glass signatures in spectroscopic survey of newly proposed lunar pyroclastic deposits. *Journal of Geophysical Research: Planets*, *119*(2), pp.355-372.

Blewett, D. T., Lucey, P. G., Hawke, B. R., & Jolliff, B. L. (1997). Clementine images of the lunar sample-return stations: Refinement of FeO and TiO2 mapping techniques. *Journal of Geophysical Research: Planets*, *102*(E7), 16319-16325.

Bussey, D. B. J., McGovern, J. A., Spudis, P. D., Neish, C. D., Noda, H., Ishihara, Y., & Sørensen, S. A. (2010). Illumination conditions of the south pole of the Moon derived using Kaguya topography. *Icarus*, *208*(2), 558-564.

Chappell, B. W. & White, A. J. R. (1974). Two contrasting granite types. *Pacific Geology,* 8, 173–174.

Christensen, P.R. and Harrison, S.T., (1993). Thermal infrared emission spectroscopy of natural surfaces: Application to desert varnish coatings on rocks. *Journal of Geophysical Research: Solid Earth*, *98*(B11), pp.19819-19834.

Conel, J. E. (1969), Infrared emissivities of silicates: Experimental results and a cloudy atmospheric model of spectral emission from condensed particulate mediums, J. Geophys. Res., 74, 1614–1634, doi:10.1029/ JB074i006p01614

Delano, J. W., & Livi, K. (1981). Lunar volcanic glasses and their constraints on mare petrogenesis. *Geochimica et Cosmochimica Acta*, *45*(11), 2137-2149.

Donaldson Hanna, K., Benavente, J., Bennett, K., Denevi, B., Dove, A., Hagerty, J., Hardgrove, C., Hayne, P., LaMee, A., Landis, M. and Osterman, D., 2023. Lunar Vulkan Imaging and Spectroscopy Explorer (Lunar-VISE). *LPI Contributions*, *2887*, p.2939.

Ehlmann, B., Klima, R.L., Bennett, C.L., Blaney, D., Bowles, N., Calcutt, S., Dickson, J., Donaldson Hanna, K., Edwards, C.S. and Green, R., 2022. Lunar Trailblazer: A pioneering SmallSat for lunar water and lunar geology. *44th COSPAR Scientific Assembly*, *44*(2548), p.301.

Frost, B. R., Barnes, C. G., Collins, W. J., Arculus, R. J., Ellis, D. J., & Frost, C. D. (2001). A geochemical classification for granitic rocks. *Journal of petrology*, *42*(11), 2033-2048.

Gillis, J. J., Jolliff, B. L., & Elphic, R. C. (2003). A revised algorithm for calculating TiO2 from Clementine UVVIS data: A synthesis of rock, soil, and remotely sensed TiO2 concentrations. *Journal of Geophysical Research: Planets*, *108*(E2).

Greenhagen, B. T., Lucey, P. G., Wyatt, M. B., Glotch, T. D., Allen, C. C., Arnold, J. A., Bandfield, J. L., Bowles, N. E., Hanna, K. L. D., Hayne, P. O., Song, E., Thomas, I. R., & Paige, D. A. (2010). Global silicate mineralogy of the moon from the diviner lunar radiometer. *Science*. https://doi.org/10.1126/science.1192196

Greenhagen, B. T., Lucey, P. G., Bandfield, J. L., Hayne, P. O., Williams, J. P., & Paige, D. A. (2011, March). The Diviner Lunar Radiometer compositional data products: Description and examples. In *42nd Annual Lunar and Planetary Science Conference* (No. 1608, p. 2679).

Greenhagen, B. T., Wagoner, C. M., Yasanayake, C. N., Donaldson Hanna, K. L., Bowles, N. E., & Lucey, P. G. (2020, March). Using mineral mixtures across the lunar mineralogy ternary to interpret LRO Diviner and future thermal infrared datasets. In *51st Annual Lunar and Planetary Science Conference* (No. 2326, p. 2171).

Glotch, T. D., Rossman, G. R., & Aharonson, O. (2007). Mid-infrared (5–100 μm) reflectance spectra and optical constants of ten phyllosilicate minerals. Icarus, 192(2), 605-622.

Glotch, T.D., Lucey, P.G., Bandfield, J.L., Greenhagen, B.T., Thomas, I.R., Elphic, R.C., Bowles, N., Wyatt, M.B., Allen, C.C., Donaldson-Hanna, K., Paige, D.A. (2010) Highly Silicic Compositions on the Moon. Science, Vol 329, p1510-1513

Gross, J., Treiman, A. H., & Mercer, C. N. (2014). Lunar feldspathic meteorites: Constraints on the geology of the lunar highlands, and the origin of the lunar crust. *Earth and Planetary Science Letters*, *388*, 318-328.

Glotch, T.D., Jawin, E.R., Greenhagen, B.T., Cahill, J.T., Lawrence, D.J., Watkins, R.N., Moriarty, D.P., Kumari, N., Li, S., Lucey, P.G. and Siegler, M.A., (2021). The scientific value of a sustained exploration program at the Aristarchus Plateau. *The Planetary Science Journal*, *2*(4), p.136.

Hagerty, J. J., Lawrence, D. J., Hawke, B. R., Vaniman, D. T., Elphic, R. C., & Feldman, W. C. (2006). Refined thorium abundances for lunar red spots: Implications for evolved, nonmare volcanism on the Moon. *Journal of Geophysical Research: Planets*, *111*(E6).

Hayne, P. O., Osterman, D. P., Donaldson Hanna, K., & Paige, D. A. (2019, December). A Compact Instrument for Mineralogical and Thermophysical Studies of the Moon from the Lunar Surface. In *AGU Fall Meeting Abstracts* (Vol. 2019, pp. P31C-3444).

Head, J.W. and Wilson, L., (2017). Generation, ascent and eruption of magma on the Moon: New insights into source depths, magma supply, intrusions and effusive/explosive eruptions (Part 2: Predicted emplacement processes and observations). *Icarus*, *283*, pp.176-223.

Hunt, G. R. (1977). Spectral signatures of particulate minerals in the visible and near infrared. Geophysics, 42(3), 501-513.

Isaacson, P. J., Sarbadhikari, A. B., Pieters, C. M., Klima, R. L., Hiroi, T., Liu, Y., & Taylor, L. A. (2011). The lunar rock and mineral characterization consortium: Deconstruction and integrated mineralogical, petrologic, and spectroscopic analyses of mare basalts. *Meteoritics & Planetary Science*, *46*(2), 228-251.

Joy, K. H., & Arai, T. (2013). Lunar meteorites: new insights into the geological history of the Moon. *Astronomy & Geophysics*, *54*(4), 4-28.

King, P.L., McMillan, P.F., Moore, G.M., Ramsey, M. and Swayze, G., (2004). Infrared spectroscopy of silicate glasses with application to natural systems. *Infrared spectroscopy in geochemistry, exploration geochemistry and remote sensing*, *33*, pp.93-133.

Klima, R. L., Pieters, C. M., Boardman, J. W., Green, R. O., Head, J. W., Isaacson, P. J., Mustard, J. F., Nettles, J. W., Petro, N. E., Staid, M. I., Sunshine, J. M., Taylor, L. A., & Tompkins, S. (2011). New insights into lunar petrology: Distribution and composition of prominent low-Ca pyroxene exposures as observed by the Moon Mineralogy Mapper (M3). *Journal of Geophysical Research E: Planets*. https://doi.org/10.1029/2010JE003719

Korotev, R. L., Jolliff, B. L., Zeigler, R. A., Gillis, J. J., & Haskin, L. A. (2003). Feldspathic lunar meteorites and their implications for compositional remote sensing of the lunar surface and the composition of the lunar crust. *Geochimica et Cosmochimica Acta*, *67*(24), 4895-4923.

Korotev, R. L. (2005). Lunar geochemistry as told by lunar meteorites. *Geochemistry*, *65*(4), 297-346.

Kumari, N., Bretzfelder, J. M., Ganesh, I., Lang, A., & Kring, D. A. (2022). Surface conditions and resource accessibility at potential Artemis landing sites 007 and 011. *The Planetary Science Journal*, *3*(9), 224.

Kumari, N., Glotch, T. D., Shirley, K. A., Greenhagen, B. T., & Byron, B. D. (2024a). Effects of space weathering on the Christiansen feature position of lunar surface materials. *Icarus*, *412*, 115976.

Kumari, N., Glotch, T.D., Williams, J.P., Sullivan, M.T., Li, S., Greenhagen, B.T., Waller, D., Powell, T., Elder, C.M., Byron, B.D. and Shirley, K.A., (2024b). Extended Silicic Volcanism in the Gruithuisen Region—Revisiting the

690 Composition and Thermophysical Properties of Gruithuisen Domes on the
691 Moon. *The Planetary Science Journal*, *5*(6), p.132.
692
693 Kumari, Nandita (2025). Characterizing Extreme Compositions on the Moon
694 Using Thermal Infrared Spectroscopy, Mendeley Data, V1, [Dataset] doi:
695 10.17632/5b5f55c6b2.1
696
697 Lawrence, D. J., Hawke, B. R., Hagerty, J. J., Elphic, R. C., Feldman, W. C.,
698 Prettyman, T. H., & Vaniman, D. T. (2005). Evidence for a high-Th, evolved
699 lithology on the Moon at Hansteen Alpha. *Geophysical Research Letters*, *32*(7).
700
701 Lee, S. K., & Stebbins, J. F. (2009). Effects of the degree of polymerization on the
702 structure of sodium silicate and aluminosilicate glasses and melts: An 17O NMR
703 study. *Geochimica et Cosmochimica Acta*, *73*(4), 1109-1119.
704
705 Li, S., & Milliken, R. E. (2017). Water on the surface of the Moon as seen by the
706 Moon Mineralogy Mapper: Distribution, abundance, and origins. *Science*
707 *advances*, *3*(9), e1701471.
708
709 Logan, L. M., G. R. Hunt, J. W. Salisbury, and S. R. Balsamo (1973),
710 Compositional implications of Christiansen frequency maximums for infrared
711 remote sensing applications, J. Geophys. Res., 78, 4983–5003,
712 doi:10.1029/JB078i023p04983.
713
714 Lucey, P. G., Blewett, D. T., & Hawke, B. R. (1998). Mapping the FeO and TiO2
715 content of the lunar surface with multispectral imagery. *Journal of Geophysical*
716 *Research: Planets*, *103*(E2), 3679-3699
717
718 McMillan, P.F., Wolf, G.H. and Poe, B.T., (1992). Vibrational spectroscopy of
719 silicate liquids and glasses. *Chemical Geology*, *96*(3-4), pp.351-366
720
721 Mazarico, E., Neumann, G. A., Smith, D. E., Zuber, M. T., & Torrence, M. H.
722 (2011). Illumination conditions of the lunar polar regions using LOLA
723 topography. *Icarus*, *211*(2), 1066-1081.
724
725 Moyen, J.F., Laurent, O., Chelle-Michou, C., Couzinié, S., Vanderhaeghe, O., Zeh,
726 A., Villaros, A., and Gardien, V., 2017. Collision vs. subduction-related
727 magmatism: two contrasting ways of granite formation and implications for crustal
728 growth. *Lithos*, *277*, pp.154-177.
729

National Research Council, Division on Engineering, Physical Sciences, Space Studies Board, & Committee on the Scientific Context for Exploration of the Moon. (2007). *The scientific context for exploration of the Moon*. National Academies Press.

O'connor, J. T. (1965). A classification for quartz-rich igneous rocks based on feldspar ratios. *US geological survey professional paper B*, *525*, 79-84.

Paige, D.A., Foote, M.C., Greenhagen, B.T., Schofield, J.T., Calcutt, S., Vasavada, A.R., Preston, D.J., Taylor, F.W., Allen, C.C., Snook, K.J., Jakosky, B.M., Murray, B.C., Soderblom, L.A., Jau, B., Loring, S., Bulharowski J., Bowles, N.E., Thomas, I.R., Sullivan, M.T., Avis, C., De Jong, E.M., Hartford, W., McCleese, D.J. (2009) The Lunar Reconnaissance Orbiter Diviner Lunar Radiometer Experiment. Space Science Reviews, Vol 150, Num 1-4, p125-160

Papike, J. J., Bence, A. E., & Lindsley, D. H. (1974). Mare basalts from the Taurus-Littrow region of the moon. In *In: Lunar Science Conference, 5th, Houston, Tex., March 18-22, 1974, Proceedings. Volume 1.(A75-39540 19-91) New York, Pergamon Press, Inc., 1974, p. 471-504.* (Vol. 5, pp. 471-504).

Papike, J. J., Hodges, F. N., Bence, A. E., Cameron, M., & Rhodes, J. M. (1976). Mare basalts: Crystal chemistry, mineralogy, and petrology. *Reviews of Geophysics*, *14*(4), 475-540.

Pieters, C. M., Taylor, L. A., Noble, S. K., Keller, L. P., Hapke, B., Morris, R. V., ... & Wentworth, S. (2000). Space weathering on airless bodies: Resolving a mystery with lunar samples. *Meteoritics & Planetary Science*, *35*(5), 1101-1107.

Ramsey, M.S. and Christensen, P.R., (1998). Mineral abundance determination: Quantitative deconvolution of thermal emission spectra. *Journal of Geophysical Research: Solid Earth*, *103*(B1), pp.577-596.

Richet, P. and Neuville, D.R., (1992). Thermodynamics of silicate melts: configurational properties. *Thermodynamic data: systematics and estimation*, pp.132-161.

Robertson, K., Milliken, R., Pieters, C., Tokle, L., Cheek, L., & Isaacson, P. (2022). Textural and compositional effects of ilmenite on the spectra of high-titanium lunar basalts. *Icarus*, *375*, 114836.

Rogers, A.D. and Aharonson, O., (2008). Mineralogical composition of sands in Meridiani Planum determined from Mars Exploration Rover data and comparison to orbital measurements. *Journal of Geophysical Research: Planets*, *113*(E6).

Ruff, S. W., Christensen, P. R., Barbera, P. W., & Anderson, D. L. (1997). Quantitative thermal emission spectroscopy of minerals: A laboratory technique for measurement and calibration. *Journal of Geophysical Research: Solid Earth*, *102*(B7), 14899-14913.

Rutherford, M.J. and Hess, P.C., (1975), March. Origin of lunar granites as immiscible liquids. In *Abstracts of the Lunar and Planetary Science Conference, volume 6, page 696,(1975)* (Vol. 6).

Ryder GR, Stoeser DB, Marvin UB, Bower JF (1975). Lunar granites with unique ternary feldspars. In: Lunar Science Conference, 6th, Houston, Tex., March 17-21.

Saal, A.E., Hauri, E.H., Cascio, M.L., Van Orman, J.A., Rutherford, M.C. and Cooper, R.F., (2008). Volatile content of lunar volcanic glasses and the presence of water in the Moon's interior. *Nature*, *454*(7201), pp.192-195.

Salisbury, J. W., Wald, A., & D'Aria, D. M. (1994). Thermal-infrared remote sensing and Kirchhoff's law: 1. Laboratory measurements. *Journal of Geophysical Research: Solid Earth*, *99*(B6), 11897-11911

Sargeant, H. M., Abernethy, F. A. J., Barber, S. J., Wright, I. P., Anand, M., Sheridan, S., & Morse, A. (2020). Hydrogen reduction of ilmenite: Towards an in situ resource utilization demonstration on the surface of the Moon. *Planetary and Space Science*, *180*, 104751.

Sato, H., Robinson, M. S., Lawrence, S. J., Denevi, B. W., Hapke, B., Jolliff, B. L., & Hiesinger, H. (2017). Lunar mare TiO2 abundances estimated from UV/Vis reflectance. *Icarus*, *296*, 216-238.

Smith, J. V., Anderson, A. T., Newton, R. C., Olsen, E. J., & Wyllie, P. J. (1970). A Petrologic Model for the Moon Based on Petrogenesis, Experimental Petrology, and Physical Properties. *The Journal of Geology*. https://doi.org/10.1086/627537

Shearer, C. K., & Papike, J. J. (1999). Magmatic evolution of the Moon. *American Mineralogist*, *84*(10), 1469-1494.

Shirley, K. A., & Glotch, T. D. (2019). Particle Size Effects on Mid-Infrared Spectra of Lunar Analog Minerals in a Simulated Lunar Environment. *Journal of Geophysical Research: Planets*. https://doi.org/10.1029/2018JE005533

Shirley, K.A., Glotch, T.D., Donaldson, O., Trelewicz, J., Yang, Y., & Zhang, H. (2023) Effects of Albedo on the MIR Emissivity of Silicates for Lunar Comarison. *Journal of Geophysical Research: Planets*. https://doi.org/10.1029/2022JE007629

Siegler, M.A., Feng, J., Lehman-Franco, K., Andrews-Hanna, J.C., Economos, R.C., Clair, M.S., Million, C., Head, J.W., Glotch, T.D. and White, M.N., (2023). Remote detection of a lunar granitic batholith at Compton–Belkovich. *Nature*, *620*(7972), pp.116-121.

Staid, M. I., Pieters, C. M., Besse, S., Boardman, J., Dhingra, D., Green, R., Head, J. W., Isaacson, P., Klima, R., Kramer, G., Mustard, J. M., Runyon, C., Sunshine, J., & Taylor, L. A. (2011). The mineralogy of late-stage lunar volcanism as observed by the Moon Mineralogy Mapper on Chandrayaan-1. *Journal of Geophysical Research E: Planets*. https://doi.org/10.1029/2010JE003735

Snyder, G. A., Taylor, L. A., & Neal, C. R. (1992). A chemical model for generating the sources of mare basalts: Combined equilibrium and fractional crystallization of the lunar magmasphere. *Geochimica et Cosmochimica Acta*, *56*(10), 3809-3823.

Tanton, L. T. E., Van Orman, J. A., Hager, B. H., & Grove, T. L. (2002). Re-examination of the lunar magma ocean cumulate overturn hypothesis: melting or mixing is required. *Earth and Planetary Science Letters*, *196*(3-4), 239-249.

Thacker, C., Liang, Y., Peng, Q., & Hess, P. (2009). The stability and major element partitioning of ilmenite and armalcolite during lunar cumulate mantle overturn. *Geochimica et Cosmochimica Acta*, *73*(3), 820-836.

Thompson, J. O., Williams, D. B., Lee, R. J., & Ramsey, M. S. (2021). Quantitative thermal emission spectroscopy at high temperatures: A laboratory approach for measurement and calibration. *Journal of Geophysical Research: Solid Earth*, *126*(7), e2021JB022157.

Thorpe, M.T. and Hurowitz, J.A., (2020). Unraveling sedimentary processes in fluvial sediments from two basalt dominated watersheds in northern Idaho, USA. *Chemical Geology*, *550*, p.119673.

Tronche, E.J., Chen, B., Gao, L., van Kan, M., Li, J., Leinenweber, K., Sanehira, T., Wang, Y. and van Westrenen, W., 2008, March. Equation of state of ilmenite at lunar pressures and temperatures. In *39th Annual Lunar and Planetary Science Conference* (No. 1391, p. 1551).

Vapnik, V., Golowich, S., & Smola, A. (1996). Support vector method for function approximation, regression estimation and signal processing. *Advances in neural information processing systems*, *9*.

Whitaker, E. A. (1972). Lunar color boundaries and their relationship to topographic features: A preliminary survey. *The Moon*, *4*, 348-355.

Wilson, L. and Head, J.W., (2017). Generation, ascent and eruption of magma on the Moon: New insights into source depths, magma supply, intrusions and effusive/explosive eruptions (Part 1: Theory). *Icarus*, *283*, pp.146-175.

Wood, J. A., Dickey Jr, J. S., Marvin, U. B., & Powell, B. N. (1970). Lunar anorthosites and a geophysical model of the moon. *Geochimica et Cosmochimica Acta Supplement*, *1*, 965.

Qiu, D., Sasaki, S., Yan, J., Ye, M., Deng, Q., Liang, F., Liu, L. and Li, F., 2023. Buried silicic volcanoes discovered in the Gruithuisen region on the Moon. *Geophysical Research Letters*, *50*(11), p.e2023GL103336.

Fig 1.

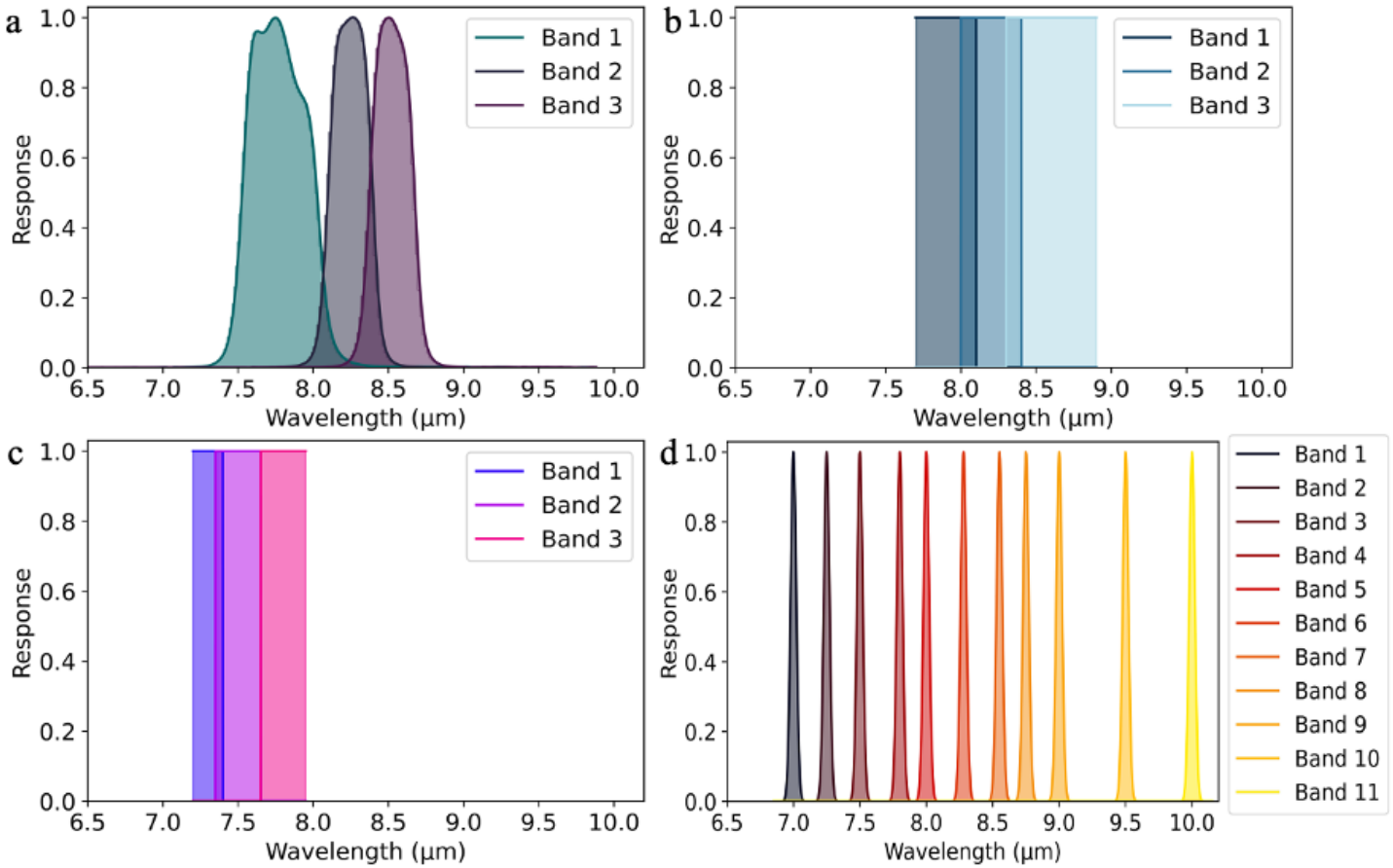
a
b
c
d
Response
Wavelength (μm)
Band 1
Band 2
Band 3
Band 4
Band 5
Band 6
Band 7
Band 8
Band 9
Band 10
Band 11
0.0
0.2
0.4
0.6
0.8
1.0
6.5
7.0
7.5
8.0
8.5
9.0
9.5
10.0

Fig 2.

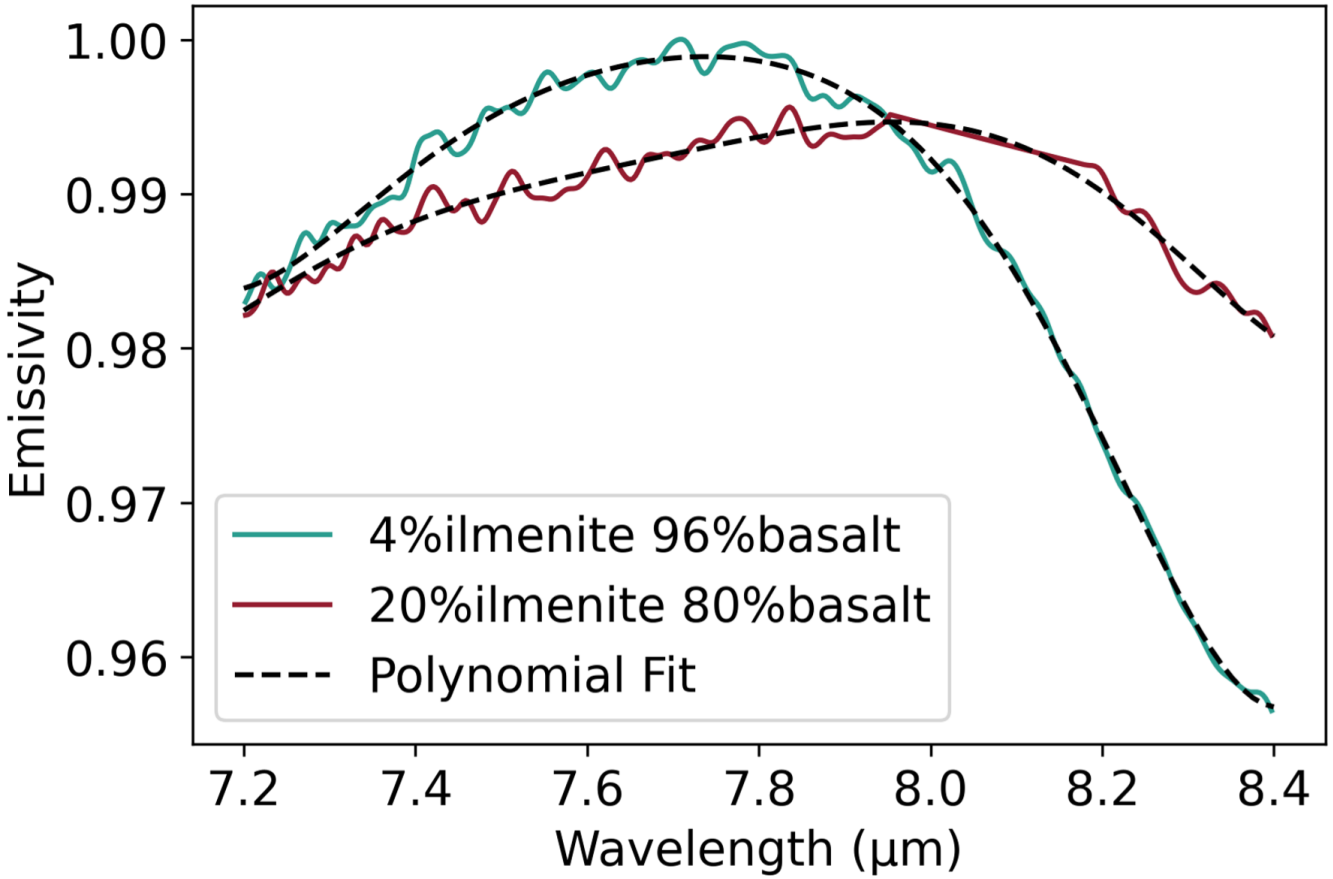
1.00
0.99
0.98
0.97
0.96
Emissivity
7.2
7.4
7.6
7.8
8.0
8.2
8.4
Wavelength (μm)
4%ilmenite 96%basalt
20%ilmenite 80%basalt
Polynomial Fit

Fig 3.

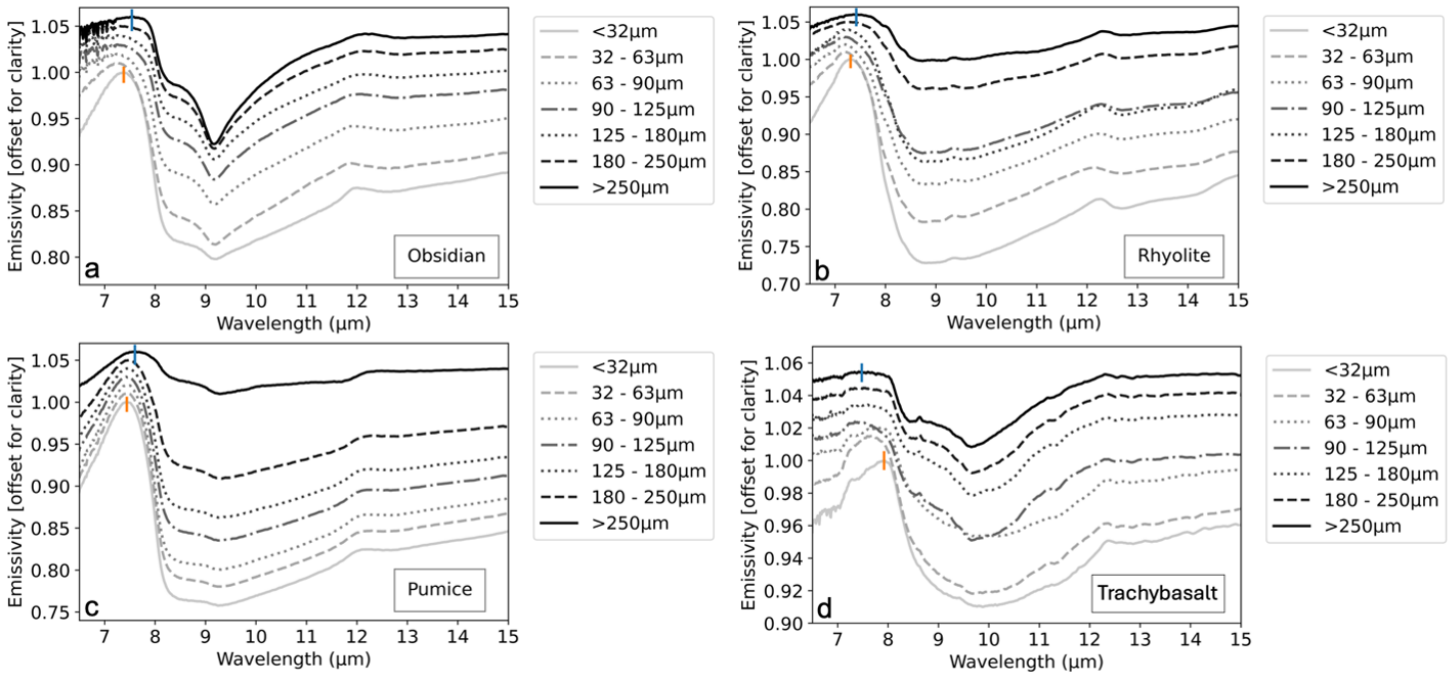
a
Obsidian
b
Rhyolite
c
Pumice
d
Trachybasalt
Emissivity [offset for clarity]
Wavelength (μm)
<32μm
32 - 63μm
63 - 90μm
90 - 125μm
125 - 180μm
180 - 250μm
>250μm

Fig 4.

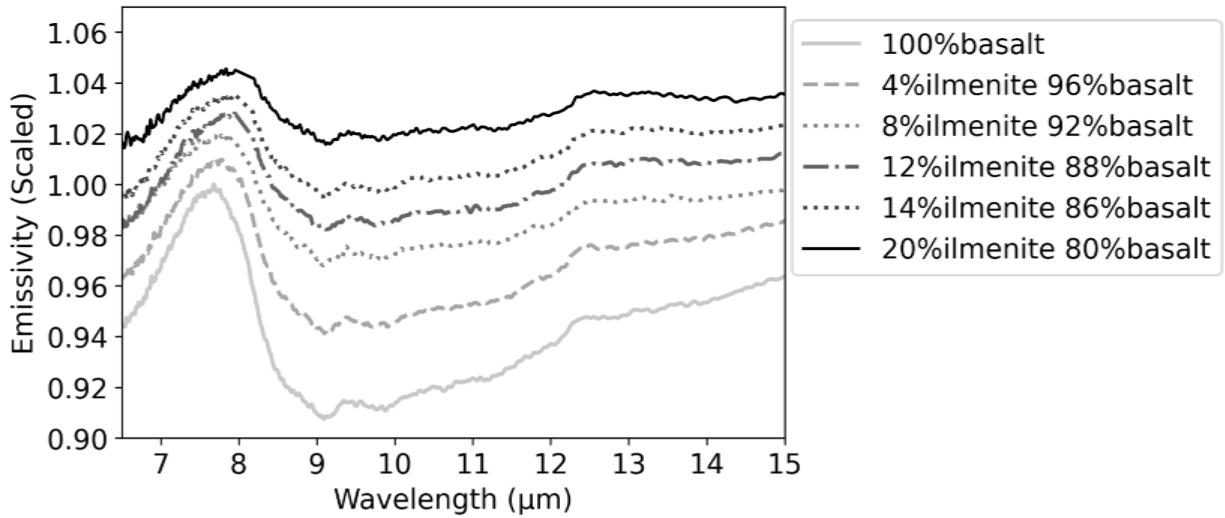
Emissivity (Scaled)
1.06
1.04
1.02
1.00
0.98
0.96
0.94
0.92
0.90
7
8
9
10
11
12
13
14
15
Wavelength (μm)
100%basalt
4%ilmenite 96%basalt
8%ilmenite 92%basalt
12%ilmenite 88%basalt
14%ilmenite 86%basalt
20%ilmenite 80%basalt

Fig 5.

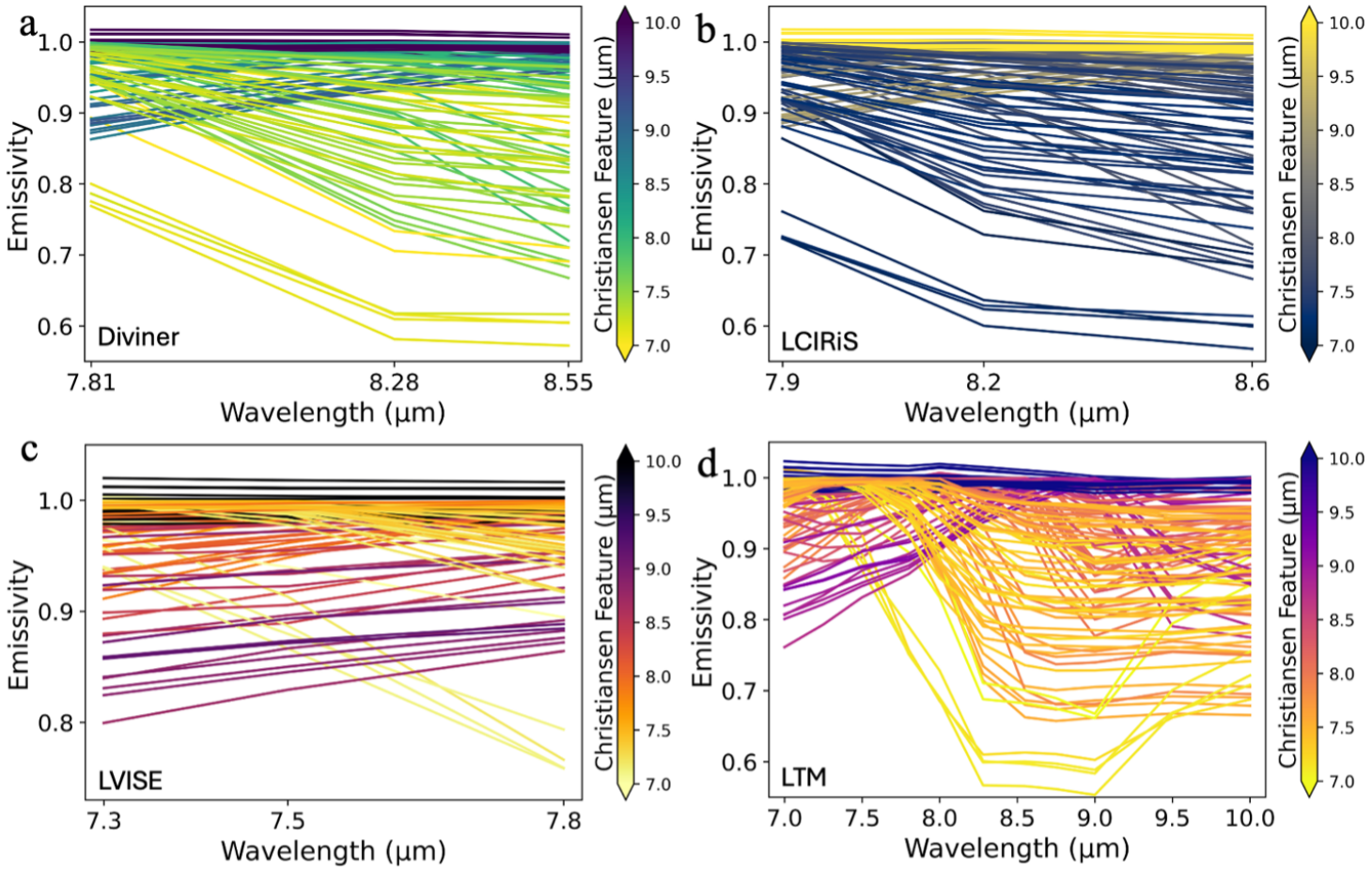
a
Diviner
Emissivity
Wavelength (μm)
Christiansen Feature (μm)
b
LCIRiS
c
LVISE
d
LTM

Fig 6.

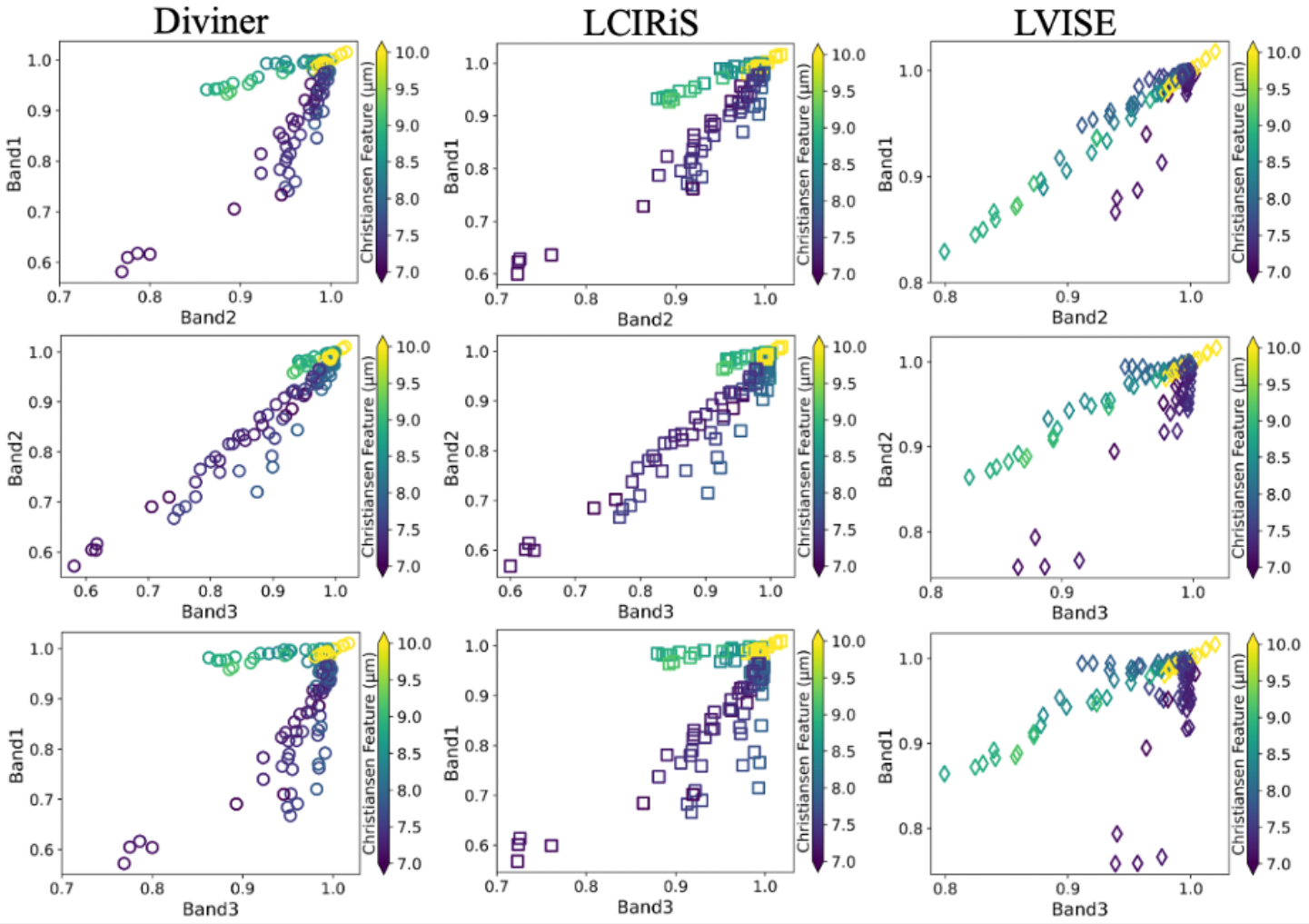
Diviner
LCIRiS
LVISE
Band1
Band2
Band3
Christiansen Feature (μm)
10.0
9.5
9.0
8.5
8.0
7.5
7.0

Fig 7.

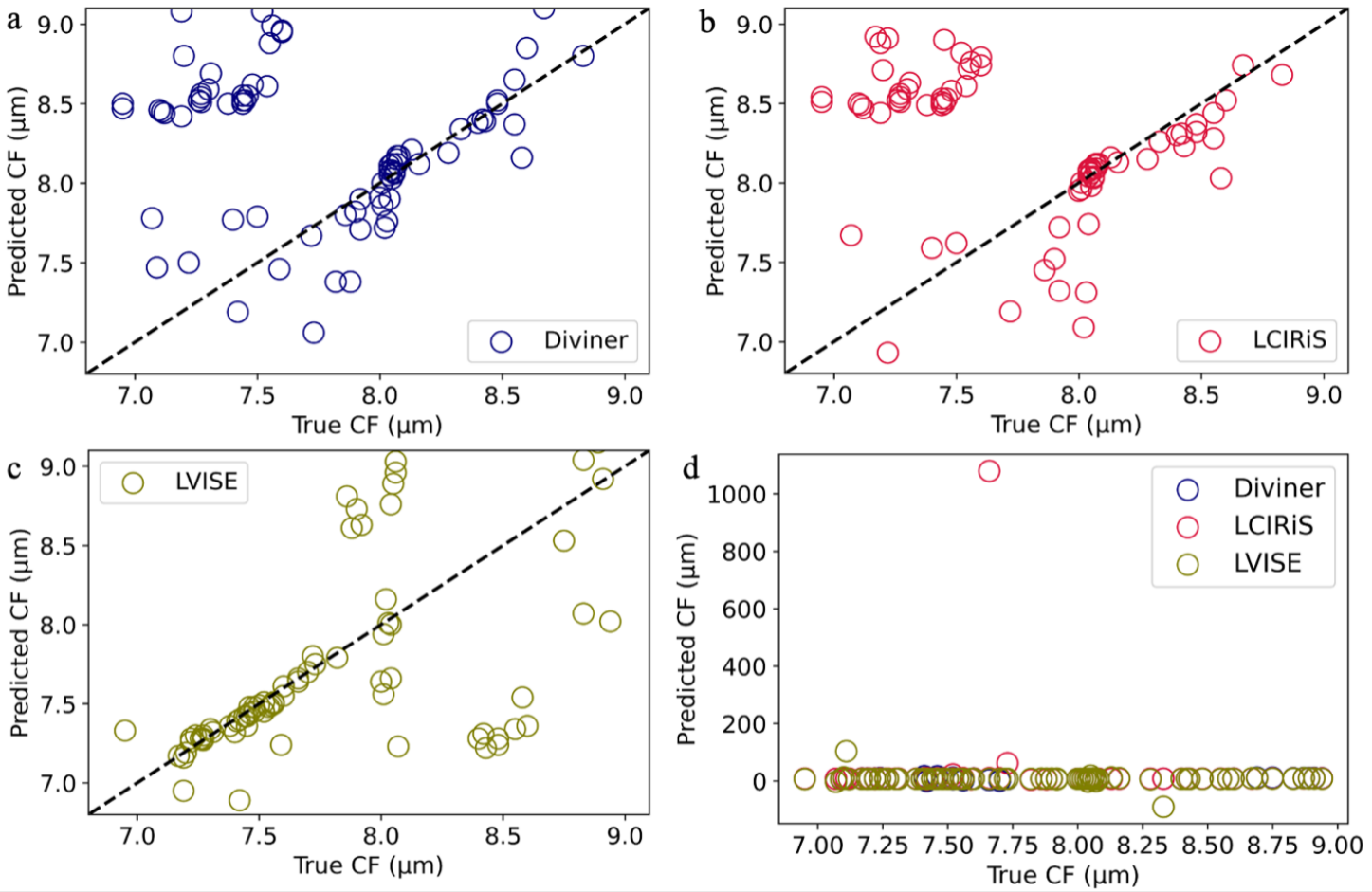
a
Predicted CF (μm)
True CF (μm)
Diviner
b
Predicted CF (μm)
True CF (μm)
LCIRiS
c
Predicted CF (μm)
True CF (μm)
LVISE
d
Predicted CF (μm)
True CF (μm)
Diviner
LCIRiS
LVISE

Fig 8.

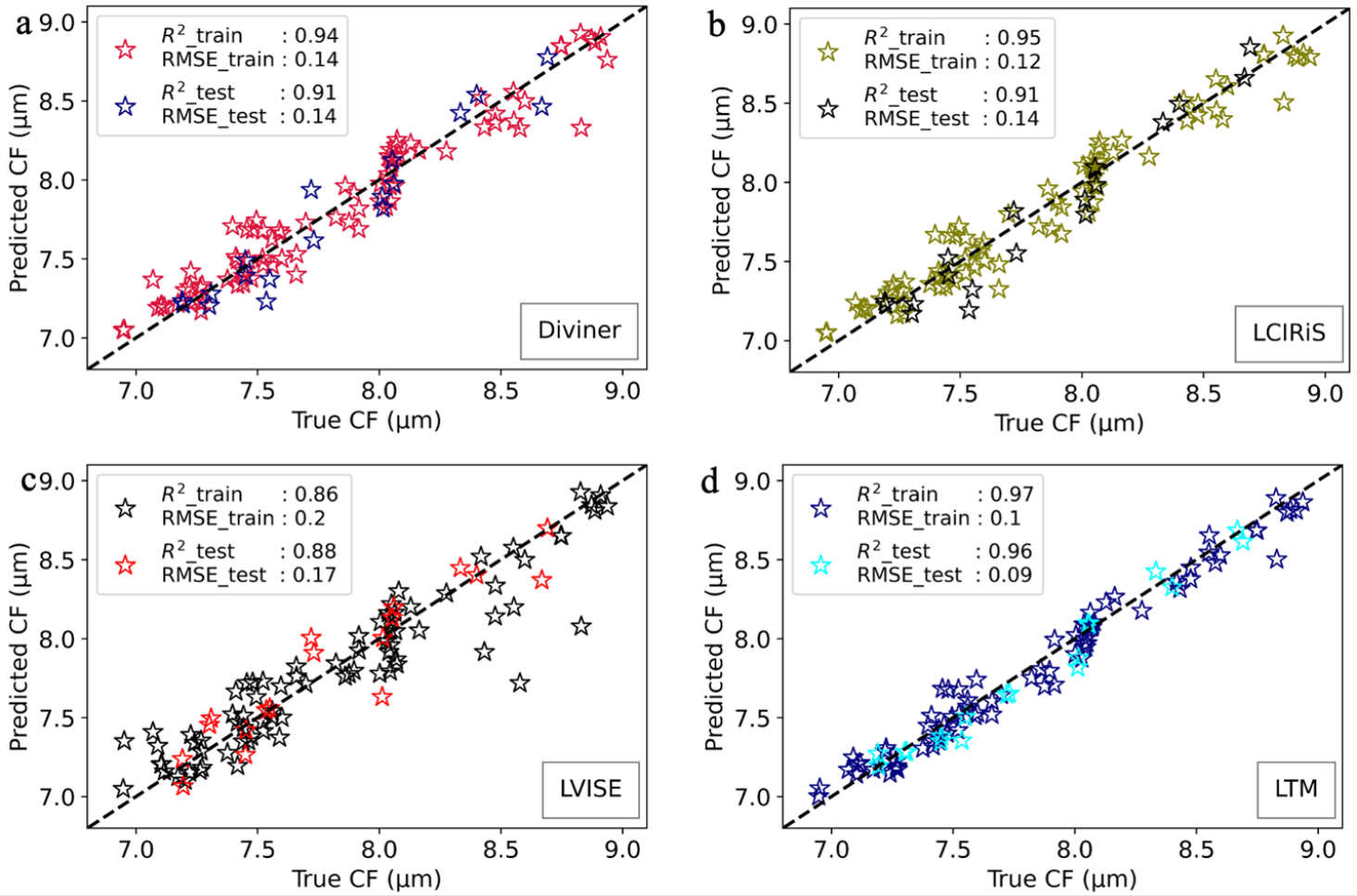
a
R^2_train : 0.94
RMSE_train : 0.14
R^2_test : 0.91
RMSE_test : 0.14
Diviner
b
R^2_train : 0.95
RMSE_train : 0.12
R^2_test : 0.91
RMSE_test : 0.14
LCIRiS
c
R^2_train : 0.86
RMSE_train : 0.2
R^2_test : 0.88
RMSE_test : 0.17
LVISE
d
R^2_train : 0.97
RMSE_train : 0.1
R^2_test : 0.96
RMSE_test : 0.09
LTM
Predicted CF (μm)
True CF (μm)
7.0
7.5
8.0
8.5
9.0

Fig 9.

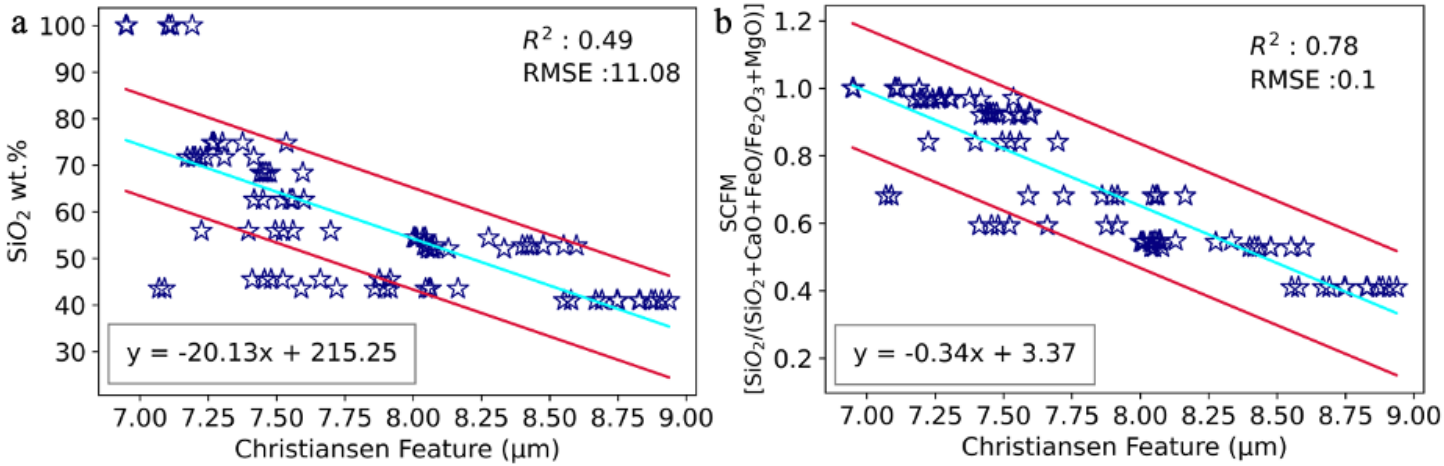
a
SiO_2 wt.%
R^2 : 0.49
RMSE :11.08
y = -20.13x + 215.25
Christiansen Feature (µm)
b
SCFM
$[SiO_2/(SiO_2+CaO+FeO/Fe_2O_3+MgO)]$
R^2 : 0.78
RMSE :0.1
y = -0.34x + 3.37
Christiansen Feature (µm)